nature astronomy

ARTICLES

https://doi.org/10.1038/s41550-021-01487-w

Check for updates

Solar wind contributions to Earth's oceans

Luke Daly[1,2,3,4]✉, Martin R. Lee[1], Lydia J. Hallis[1], Hope A. Ishii[5], John P. Bradley[5], Phillip. A. Bland[2], David W. Saxey[6], Denis Fougerouse[2,6], William D. A. Rickard[6], Lucy V. Forman[2], Nicholas E. Timms[2], Fred Jourdan[2], Steven M. Reddy[2,6], Tobias Salge[7], Zakaria Quadir[8,9], Evangelos Christou[1], Morgan A. Cox[2], Jeffrey A. Aguiar[10,11], Khalid Hattar[12], Anthony Monterrosa[12], Lindsay P. Keller[13], Roy Christoffersen[14], Catherine A. Dukes[15], Mark J. Loeffler[16] and Michelle S. Thompson[17]

The isotopic composition of water in Earth's oceans is challenging to recreate using a plausible mixture of known extraterrestrial sources such as asteroids—an additional isotopically light reservoir is required. The Sun's solar wind could provide an answer to balance Earth's water budget. We used atom probe tomography to directly observe an average ~1 mol% enrichment in water and hydroxyls in the solar-wind-irradiated rim of an olivine grain from the S-type asteroid Itokawa. We also experimentally confirm that H^+ irradiation of silicate mineral surfaces produces water molecules. These results suggest that the Itokawa regolith could contain ~20 l m^{-3} of solar-wind-derived water and that such water reservoirs are probably ubiquitous on airless worlds throughout our Galaxy. The production of this isotopically light water reservoir by solar wind implantation into fine-grained silicates may have been a particularly important process in the early Solar System, potentially providing a means to recreate Earth's current water isotope ratios.

The origin of Earth's water and volatile budget is a topic of considerable debate in planetary science[1–10]. Most current dynamical models of Earth's formation assume that the majority of Earth's water and other volatiles was added later from an exogenous source[1–4]. That volatile source shared a common parent population with C-type asteroids that is probably located in the Jupiter–Saturn region and beyond[11–14]. C-type asteroids are thought to be the parent bodies of carbonaceous (C) chondrite meteorites as they exhibit similar reflectance spectra, in particular the CR, CM and CI chondrites[15], which can contain up to 10 wt% H_2O (Table 1)[9]. Although the D/H isotope ratios of C-chondrite meteorites are a closer fit to the Earth than to comets or other meteorite types, with CMs being a particularly close match (Table 1)[2,16], the Earth's mantle and standard mean ocean water (SMOW) are lighter in D/H (ref. [17]) than the average of CI, CR and CM chondrite groups (for example, refs. [1,16,18]; Table 1). Given the diversity of water-rich C-chondrites in the meteorite record, it is unlikely that CM-like asteroids alone delivered all of Earth's water. Thus, as they are the most water-rich meteorites[9], the CIs, CRs and CMs are believed to represent the majority of Earth's chondritic water component. Although recent studies of nominally anhydrous minerals from enstatite chondrites[10] and Itokawa particles[19] suggest that these materials may be more water-rich than previously thought, they contain sufficient water for only the lowest estimate of Earth's water budget (Table 1). D/H ratios of the Earth's deep mantle are even lighter than SMOW (Table 1)[2]; recent analysis of volcanically exhumed material indicates that a component of isotopically light, solar-like D/H may be extant in the primitive mantle (Table 1)[6]. In addition, the bulk D/H ratio of the Earth may have increased from its initial value over the last 4.5 Gyr, potentially due to a preferential loss of the lighter hydrogen isotope to space[20]. However, increasing the D/H ratio via this mechanism is challenging to reconcile with extraterrestrial delivery of other isotope systems from C-type material, such as nitrogen[3]. Nevertheless, the volatile isotopic composition of the Earth is an enigma, and it is likely that at least one other light isotope reservoir contributed to our planet's water budget—the Sun, for example, and/or the solar nebula.

The Sun could provide this additional reservoir, as it is isotopically light compared with SMOW and the bulk Earth (Table 1)[4]. It has been suggested that H adsorption onto mineral grain surfaces in the nebula[21] or dissolution of nebular H_2 into Earth's magma ocean[7,22] could have contributed a solar nebula D/H component. However, there are substantial issues with these models[3], and the abundance of H deliverable by these mechanisms are unconstrained and would only be a contributing factor while the gaseous nebula is present. A late veneer of the final 0.5 ± 0.25% of Earth's mass[23–25], post core formation and after the gas disk had dissipated, is likely to have contributed some of Earth's water from a predominantly chondritic source[11–14], but may still require a light D/H reservoir.

[1]School of Geographical and Earth Sciences, University of Glasgow, Glasgow, UK. [2]Space Science and Technology Centre, School of Earth and Planetary Sciences, Curtin University, Perth, Western Australia, Australia. [3]Australian Centre for Microscopy and Microanalysis, University of Sydney, Sydney, New South Wales, Australia. [4]Department of Materials, University of Oxford, Oxford, UK. [5]Hawaii Institute of Geophysics and Planetology, University of Hawai'i at Mānoa, Honolulu, HI, USA. [6]Geoscience Atom Probe Facility, John de Laeter Centre, Curtin University, Perth, Western Australia, Australia. [7]Imaging and Analysis Centre, Natural History Museum, London, UK. [8]School of Civil and Mechanical Engineering, Faculty of Science & Engineering, Curtin University, Perth, Western Australia, Australia. [9]Microscopy & Microanalysis Facility, John de Laeter Centre, Curtin University, Perth, Western Australia, Australia. [10]Nuclear Materials Department, Idaho National Laboratory, Idaho Falls, ID, USA. [11]Advanced Technology Center, Lockheed Martin, Palo Alto, CA, USA. [12]Sandia National Laboratories, Albuquerque, NM, USA. [13]Robert M Walker Laboratory for Space Science, Code KR, Astromaterials Research and Exploration Science, NASA Johnson Space Center, Houston, TX, USA. [14]Jacobs, NASA Johnson Space Center, Houston, TX, USA. [15]Laboratory for Astrophysics and Surface Physics, University of Virginia, Charlottesville, VA, USA. [16]Department of Astronomy and Planetary Science, Northern Arizona University, Flagstaff, AZ, USA. [17]Department of Earth, Atmospheric and Planetary Sciences, Purdue University, West Lafayette, IN, USA. ✉e-mail: luke.daly@glasgow.ac.uk

Table 1 | Summary of the D/H ratio and water abundance of extraterrestrial and terrestrial materials

Water reservoirs	Water abundance (wt%)	Mean atomic mass	Water abundance (mol%)	D/H ratio (10^{-6})
Extraterrestrial				
CM meteorites	1.6–12.9	24	2.1–16.4	148 ± 20
CI meteorites	1.6–12.9	24	2.1–16.4	168 ± 1
CR meteorites	1.6–12.9	24	2.1–16.4	257 ± 20
Enstatite chondrites	0.1–0.5	25.6	0.1–0.8	131 ± 8
Itokawa/ordinary chondrites	0.1–0.5	24.4	0.1–0.7	135 ± 2
Solar wind	-	-	-	0.2–20 ± 4
Solar-wind-irradiated <10 μm Itokawa olivine	0.1–1.2	24	0.1–1.6	0.2–20 ± 4
Terrestrial				
SMOW	-	-	-	156 ± 0.1
Bulk Silicate Earth	0.6–3.6	21.2	0.9–5.2	149 ± 3
Earth's Deep Mantle	0.1–1	21.2	0.2–1.2	122 ± 5

Data are from this study and refs. [1,2,4,6,10,16,18,19,26,78,80,81,83,84]. Uncertainties are 1σ.

Intriguingly, volatile isotope ratios of hydrogen from the solar wind (for example, D/H = 2×10^{-7}; Table 1 and ref. [26]) and the surfaces of materials that have been irradiated by the solar wind, such as the samples recovered from NASA's GENESIS mission[27], have D/H isotope ratios consistent with the protosun and protosolar nebula[26,27]. The composition of the solar photosphere, and by extension the solar wind, is 96% H and 4% He, with the remaining ions composed of all elements in their solar abundance ratios[28,29].

It has been demonstrated by observation and experimentation that solar wind irradiation of rocky materials results in a reaction between H ions and silicate minerals to produce OH and water[5,30–34]. These molecules may become trapped in the 20- to 200-nm-thick damage layer induced by solar wind irradiation and other space weathering processes[30]. This phenomenon could explain why the regoliths of airless worlds such as the Moon, which were once thought to be anhydrous, contain several per cent H_2O[35–37]. Implantation of solar H may also explain why nominally anhydrous minerals in asteroids have water abundances of several hundred parts per million[10,19] by weight. Clear evidence for these reactions also comes from the detection of OH bonds and inferred water contents of up to 1 mol%, where mol% is equivalent to the percentage of water molecules (the sum total of H, OH and H_2O ions per 100 atoms of a material; see Methods) in the solar-wind-irradiated surfaces of interplanetary dust particles (IDPs), as well as the production of water in minerals during laboratory space weathering experiments[30,33]. These lines of evidence hint that a volatile reservoir isotopically similar to the solar wind may have been present in the Solar System and contributed to Earth's oceans. One potentially important source of such water, the contribution of which has yet to be quantitatively evaluated, is the regolith of silicate-rich asteroids and other fine-grained extraterrestrial materials such as IDPs and the matrix of primitive chondrite meteorites. Such materials comprise ~99% of the present-day extraterrestrial mass flux[38]; they were produced in high quantities through a variety of mechanisms including impacts between planetesimals, active outgassing or disruptive outbursts from comets and asteroids, and bombardment by and collisions between IDPs in the radiation-rich debris disk stage of a protoplanetary disk[39–42], and so also during the late veneer stage of accretion of the terrestrial planets.

Atom probe tomography (APT) is a quantitative analytical technique capable of measuring the abundance of water and OH molecules within minerals in three dimensions at subnanometre resolution[43]. We utilized APT to measure water abundances of space-weathered surfaces on two sides of a particle from the asteroid Itokawa (RA-QD02_0279) (Methods, Fig. 1 and Extended Data Figs. 1–7) that was returned to Earth by the Japanese Aerospace Exploration Agency (JAXA) Hayabusa mission in 2011[44]. Our Itokawa APT data (Fig. 2 and Extended Data Figs. 1–7) are supported by results from analyses of the same particle by scanning electron microscopy (SEM) (Fig. 1a,b and Extended Data Figs. 1 and 2) and transmission electron microscopy (TEM) (Fig. 1c–e). In addition, APT measurements of four experiments using San Carlos olivine (SCO) standard reference materials support this work. One pristine SCO sample was exposed to the laboratory atmosphere (PSCO), one was irradiated with He^+ (HeSCO) at 4 keV and a third and fourth was irradiated with D^+ (DSCO) at 1 and 5 keV (Fig. 2d–j, Extended Data Figs. 5d and 8 and Methods). The energies used during the D^+ and He^+ irradiation experiments are consistent with that of the solar wind.

SEM images of the Itokawa grain show that its surface has an angular, pristine appearance and is free of micrometeorite impact craters (Fig. 1a,b and Extended Data Figs. 1 and 2). TEM images of the particle indicate that it has a 40- to 50-nm-thick solar-wind-irradiated rim that is crystalline and exhibits slight variations in density (Fig. 1c–e). The space-weathered rim was sensitive to irradiation by the electron beam, resulting in a change in contrast relative to the rest of the grain, which could be due to its volatile enrichment. No Fe nanoparticles were observed (Fig. 1c–e) in contrast to reports from other Itokawa grains[45] and APT analyses of lunar ilmenite[46]. The properties of the solar-wind-irradiated surface and rim of this grain indicate that its space-weathering features could be immature, maybe because it was exposed for a shorter period than other previously characterized space-weathered Itokawa grains[45].

APT results from the Itokawa grain reveal that OH and water are enriched in the rims on both sides of the particle by 0.1–1.6 ± 0.05 mol% above background (Fig. 2a–c, Extended Data Figs. 3 and 4, and Methods). The depth of water implantation (40–180 nm) is consistent with Monte Carlo simulations of the penetration depth of solar-wind-derived H^+ into silicate minerals at heliocentric distances of Itokawa[47], and with our TEM observations (Fig. 1c–e).

APT data revealed that there was no OH or H_2O enrichment in the near-surface profile of the PSCO grains, indicating that the signal in the Itokawa particle is not an artefact of sample handling or laboratory analysis (Extended Data Fig. 8v–x). In contrast, the outermost 50 nm of the DSCO sample is enriched with respect to D, D_2, DO and D_2O (Fig. 2d–j and Extended Data Figs. 4d and 8a–u). While this rim is similar in thickness to the space-weathered profile of Itokawa, importantly no H was generated by laboratory

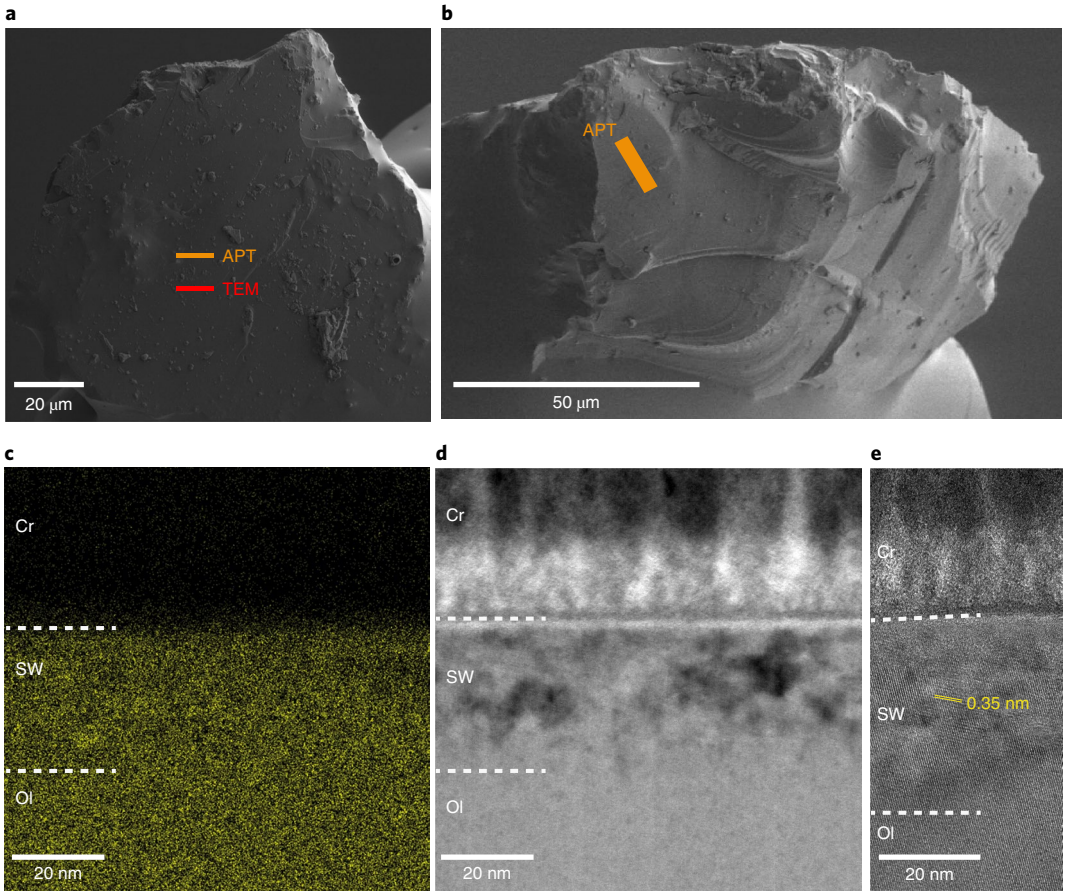

Fig. 1 | SEM and TEM analyses of the space-weathered surface of Itokawa particle RA_QD02_0279. a,**b**, Secondary electron images of the front (**a**) and rear (**b**) surfaces of the particle. Coloured boxes indicate extraction locations of TEM (red) and APT (orange) samples. **c**, TEM energy-dispersive X-ray spectroscopy (EDS) Fe Kα X-ray map of the grain surface. Fe nanoparticles are absent, and subtle variations in the Fe X-ray signal are due to contrasting density through the rim, not compositional variations. The protective Cr coat, space-weathered (SW) rim and unweathered olivine (Ol) are labelled. **d**, Bright-field TEM image of the outermost part of the olivine grain and Cr coat. The 50-nm-thick SW rim is readily apparent beneath the grain surface and is delineated by two dashed white lines. The patchy contrast of the rim indicates variations in the intensity of electron scattering and density, but not in composition. **e**, High-angle annular dark field (HAADF) TEM image of the protective Cr coat, SW rim and Ol. Lattice fringes with a 0.35 nm spacing, probably {120} planes (yellow), extend through the SW rim indicating that it is, at least in part, crystalline.

irradiation, and a substantially lower H and OH signal was observed across the DSCO rim relative to the unirradiated bulk olivine portion of the DSCO sample (Fig. 2d–j and Extended Data Figs. 4d and 8a–u). This DSCO result further confirms that heavy water can be generated by D^+ irradiation of silicate mineral surfaces, and therefore, H^+ irradiation would similarly generate water[5,30–34]. Moreover, the absence of H and OH in the rim of the D-irradiated grain (Fig. 2d–j, and Extended Data Figs. 4 and 8a–u) indicates that isotopic exchange of an irradiated grain surface with the terrestrial atmosphere is minimal, at least over curatorial timescales. Thus, APT results acquired from the SCO standard reference materials confirm that the Itokawa results are not a consequence of sample preparation or terrestrial contamination and therefore must be due to extraterrestrial processes, specifically solar wind implantation of volatiles (Methods, Fig. 2d–j and Extended Data Figs. 4d and 8).

Despite the immature space weathering of the Itokawa grain (Fig. 1 and Extended Data Figs. 1 and 2; ref. [45]), we observe an implanted water enrichment (0.1–1.6 ± 0.05 mol%) in its rims (Fig. 2a–c and Extended Data Figs. 3 and 4a–c). These water abundances are similar to those detected in space-weathered rims of a similar thickness on the surfaces of silicate grains from IDPs[30]. Thus, comparable water abundances have now been determined for two solar-wind-irradiated materials using two different techniques, giving confidence in the enrichment level provided by both sets of measurements. This measured water enrichment is interpreted as the 'saturated' value, where solar wind implantation is in equilibrium with volatile loss in the space environment through solar heating and prolonged (~8 Myr for Itokawa[48]) exposure to a vacuum[49]. Thus, using this water enrichment value (0.1–1.6 ± 0.05 mol%) and assuming space-weathered rim thicknesses of 40–200 nm (refs. [30,47,50]) for olivine and other silicate minerals, the overall water abundance imbibed into olivine grains of various sizes can be estimated (Fig. 3 and Methods). A space-weathered spherical particle with a diameter of 100 μm, typical for most Itokawa regolith grains[44,45,47], would contain ~0.01 mol% solar-wind-derived water (Fig. 3). Assuming that water enrichment by the solar wind is consistent between grains and minerals that comprise the regolith of Itokawa, every 1 m^3 of Itokawa regolith could contain up to ~201 of solar-wind-derived water. As such, solar-wind-irradiated silicate minerals may represent a substantial renewable source of water on airless worlds throughout the Galaxy.

The abundance of water within a particular grain will depend on its indigenous water constrained by its mineralogy and source, and the abundance of solar-wind-derived water, which is dependent on the grain size and shape of the particles. Most terrestrial olivine contains ~0.001–0.01 mol% water (for example, ref. [51]).

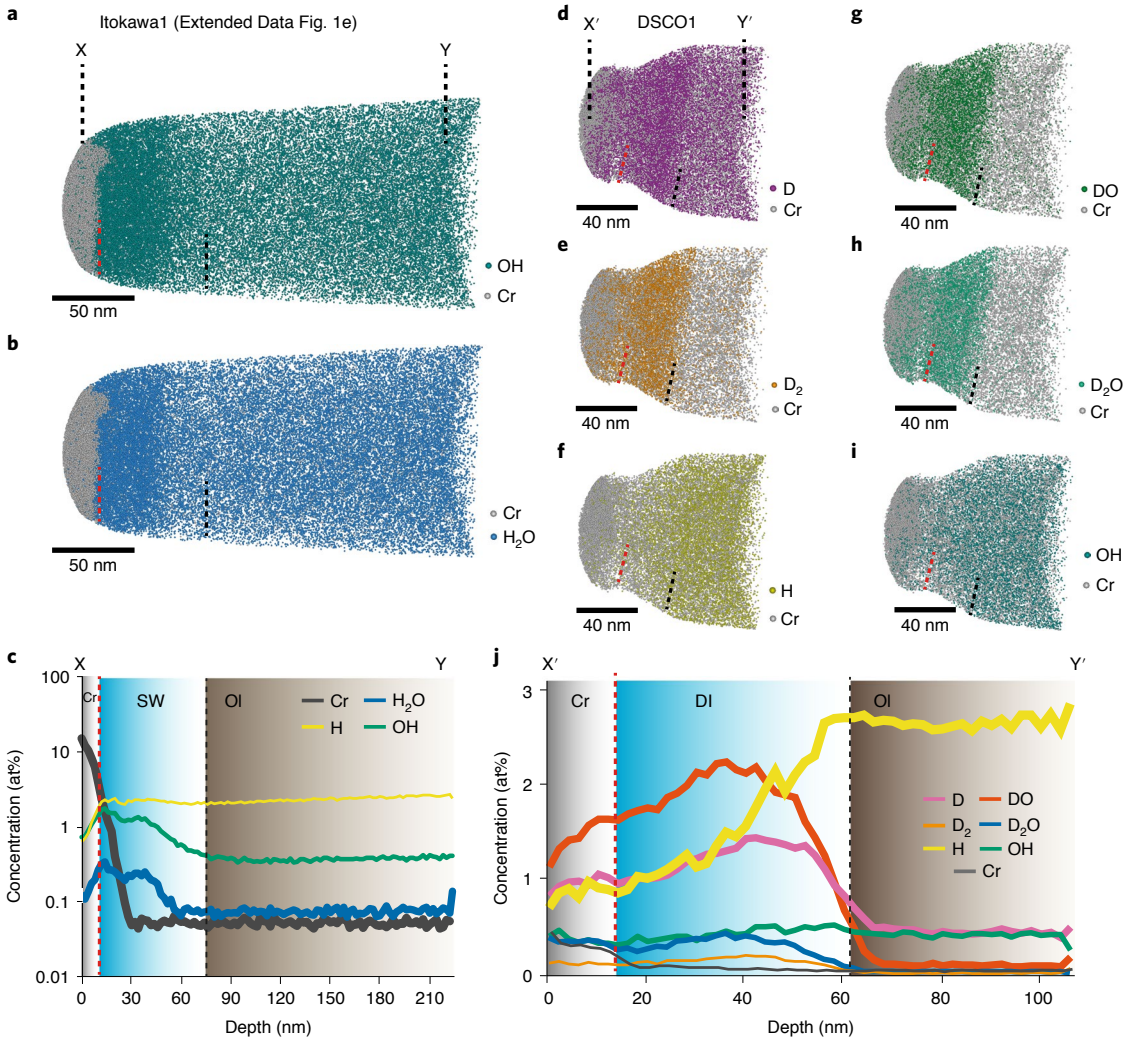

Fig. 2 | Representative APT data from Itokawa particle RA_QD02_0279 and DSCO. a–j, All datasets extend from the Cr protective layer (grey spheres) through RA_QD02_0279's SW surface (**a**–**c**) or through DSCO's D-irradiated surface (**d**–**j**) into OI. **a**, APT measurement of the 3D distribution of Cr and OH ions. **b**, APT measurement of the 3D distribution of Cr and H_2O ions. **c**, Concentration of ions (in at%; number of atoms per 100 atoms) with depth across the Cr capping layer (grey shaded region) SW rim (blue shaded region) and the non-space-weathered OI (brown shaded region) along X–Y in **a**, revealing variations in the abundances of Cr, H, OH and H_2O ions. The maximum water abundance within the SW rim is 1.6 mol% and the average water abundance across the SW rim is 0.8 mol%. Line widths have been adjusted to represent the 1σ uncertainty and depth profiles are absolute abundances not relative concentrations (Supplementary Data 1). The boundary between the Cr and SW layers is marked by a vertical dashed red line and the boundary between the SW and OI layers is marked by a vertical black dashed line. **d**–**i**, APT measurements of the 3D distribution of ions through a typical DSCO sample. In all images, the Cr ions are shown together with one other ion, and the boundaries between layers are indicated by the red and black dashed lines. **d**, D ions. **e**, D_2 ions. **f**, H ions. **g**, DO ions. **h**, D_2O ions. **i**, OH ions. **j**, Concentration of ions with depth across the Cr capping layer (grey shaded region) deuterium-irradiated rim (DI, blue shaded region) and the non-deuterium-irradiated OI (brown shaded region) along X′–Y′ in **d**, revealing the variation in the abundance of Cr, D, D_2, DO, D_2O, H and OH ions. Line widths have been adjusted to represent the 1σ uncertainty and depth profiles are absolute abundances not relative concentrations (Supplementary Data 1). The boundary between the Cr and DI layers is marked by a vertical dashed red line and the boundary between the DI and OI layers is marked by a vertical black dashed line.

Itokawa regolith and ordinary chondrite silicates may be more water rich throughout, where pyroxene grains from Itokawa, and pyroxene and olivine grains within ordinary chondrites and chondrule glasses within enstatite chondrites, have measured water contents of 0.016–0.0998 mol% (refs. [10,19]). Thus, assuming spherical particles >100 µm in size, the solar wind contribution to their overall water budget would be <50%. For particles ~100 µm in diameter, the solar-wind-derived water of a particle would represent at least half of its total water budget, producing a nominally water-poor particle with an isotopic signal between the heavier chondritic values[1,16] and lighter solar values[4,27–29]. However, the solar-wind-derived component would constitute 0.1–1.6 mol% water in particles <10 µm in diameter (Fig. 3), thus close to 100% of the water present in the grain.

Particle sizes of <10 µm are typical for the matrices of primitive chondritic meteorites[52,53], IDPs[54] and cometary fragments from Wild 2 recovered by the Stardust mission[55]. At the present day, ~30,000 t of small particles (submicrometre–millimetre with a peak at 200 µm) thought to originate from comets, asteroids and IDPs fall to Earth each year[56–58] representing 99% of the annual delivery of extraterrestrial matter;[38] IDPs alone contribute ~1% of Earth's current annual extraterrestrial input[58]. In addition, coarse >100 µm highly porous aggregates such as IDPs[54] and fragments of chondritic matrix[52,53] that have a larger surface area to volume ratio would also

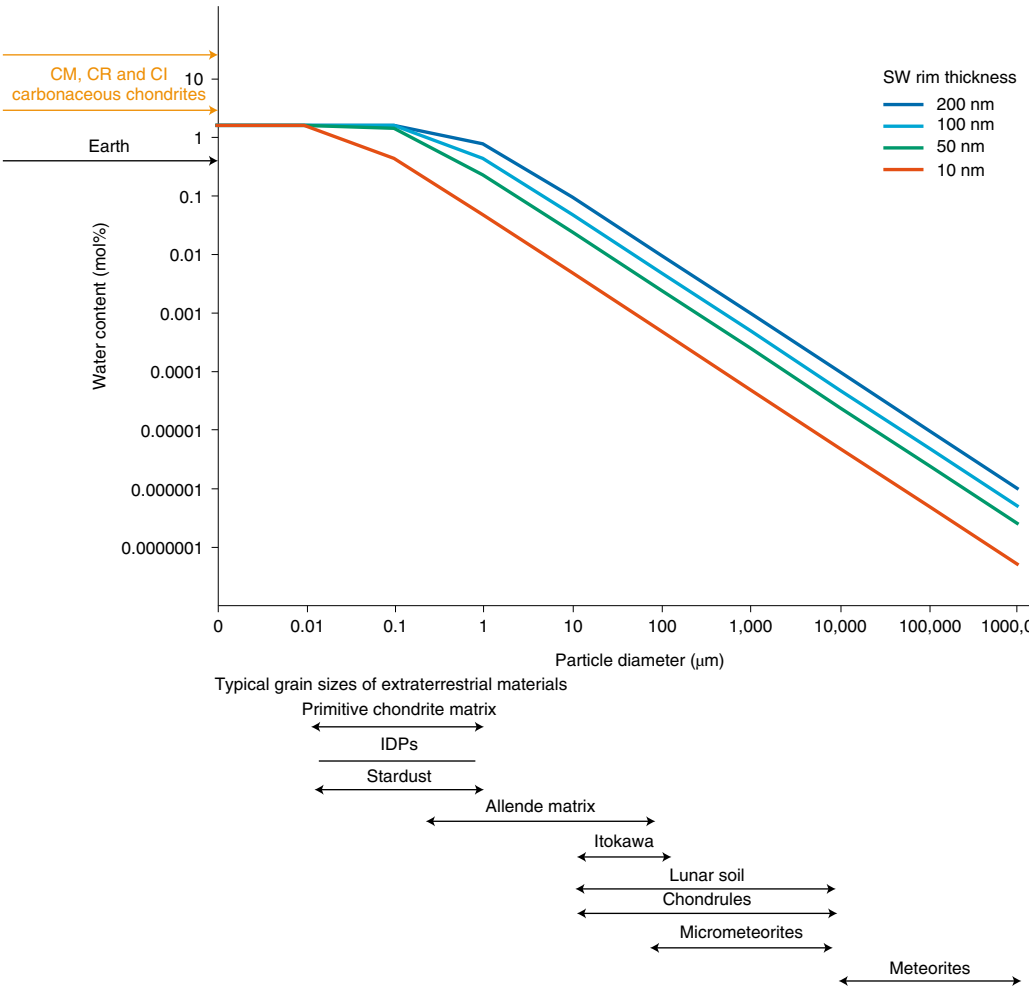

Fig. 3 | Graph of particle diameter versus the abundance of water generated by solar wind irradiation. A variety of extraterrestrial materials are shown, each of which has an SW rim of different thickness: lunar soil (200 nm); IDPs and maturely SW Itokawa particles (100 nm); the sub-mature Itokawa grain in this study (50 nm) and a very thin SW surface (10 nm). Representative grain sizes and water abundances for different extraterrestrial materials are labelled below the graph. We assumed a spherical particle in all cases, and as such they represent the minimum solar-wind-derived water contents for particles of these diameters. Fractal grains will have a larger surface area and therefore a greater solar-wind-derived water component. Particles <1 μm can entrain and store several mol% of water derived from solar wind irradiation.

be substantially enriched in solar-wind-derived water and may have comparable solar-wind-derived water contents to <200 nm isolated grains. Therefore, isolated grains in interplanetary space of similar size, irradiated by the solar wind, could represent an important source of isotopically light water in the Solar System.

Assuming that this particle size distribution is also representative of the debris disk stage of Solar System formation, following the dissipation of the solar nebula when the disk would have become transparent, then fine-grained and/or porous particles in the IDP–chondritic matrix size range that are isotopically light and water rich may have been accreted alongside planetesimal sized objects during the late veneer to contribute the final 0.5 ± 0.25% of Earth's mass. As many of these particles are nanocomposites of (organic) carbon and silicate minerals[30,59], solar wind production of water at their surfaces may have been accompanied by diversification of molecular chemistry. However, for fine-grained materials irradiated by the solar wind to have contributed substantially to the Earth's late veneer, dust generation at this time period must have been greater than at the present day. Indeed, observations of dusty debris disks in our Galaxy by WISE indicate that between 10^{-1} and 10^{-4} Earth masses is present as micrometre-sized dust[60]. Similar dust abundances are thought to have been present during this stage of our own Solar System's formation. The dust would then have been accreted alongside large chondritic asteroids. Very little dust, particularly fine-grained materials, would have remained in the protoplanetary disk once the nebular gas had dissipated[61]. However, substantial amounts of dust are observed in current debris disks around nascent planetary systems[41] that probably formed by giant impacts (for example, refs. [39–41]), collisional cascades between ~100-km-sized bodies resulting in runaway collisions between progressively smaller asteroids and resulting in their complete disaggregation into micrometre-sized dust[60], as well as active outgassing and disruptive outbursts from primitive asteroids and comets[42]. In addition, numerical modelling of the evolution of IDP size suggests that fine-grained dust in the ~5 μm size range dominates the mass fraction of dust in the inner Solar System at the expense of larger IDPs[42]. This would provide an abundance of fine-grained particles implanted with a major component of solar-wind-derived water. Thus, the abundance of fine-grained particles such as IDPs during this time period is expected to be orders of magnitude greater than at the present day[56,62]. This newly formed dust would subsequently have been exposed to the solar wind to produce water before it was (re)accreted by the terrestrial planets and asteroids. Another consideration is that during the debris disk stage of the early Solar System, particles would have experienced

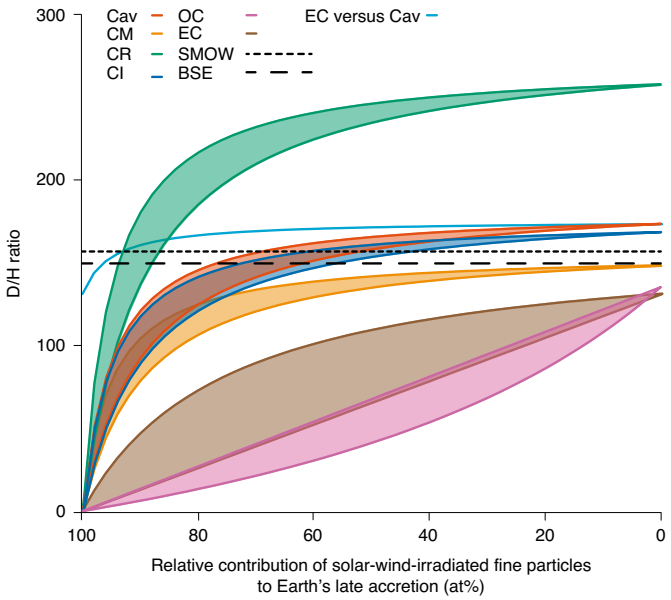

Fig. 4 | Diagram of the D/H ratio that results from mixing solar-wind-irradiated fine-grained particles and chondritic water reservoirs. The D/H ratio plot is generated by mixing water reservoirs of carbonaceous chondrite (where Cav is the average of CR, CI and CM D/H = 0.000173 (refs. [1,16]); water abundance = 2–16 mol% (ref. [9])), ordinary chondrite (OC)[19] and enstatite chondrite (EC)[10] material, and small (<100 μm) SW particles (D/H = 0.0000002 (ref, [26]); water abundance = 0.1–1.6 mol%) that can reproduce the SMOW and bulk silicate Earth (BSE) D/H ratio[1,17] (Supplementary Data 3). The upper and lower bounds of each coloured field represent the upper and lower limits of the water content within the chondrites and solar-wind-irradiated particles. The relative mass contributions that span BSE and SMOW D/H ratios indicate the range of potential mixtures of the extraterrestrial water reservoirs that could generate the present-day D/H of Earth's oceans. We also plot the D/H ratio produced by the mixture of EC versus Cav material.

much more intense solar wind irradiation than at the present day because, while the early Sun was much fainter during its formation, the solar wind flux was higher and more energetic[63,64]. This enhanced solar wind flux would be particularly important during the energetic T-Tauri stage of our Sun[56]. Therefore, exposed small particles would have accumulated more water than at the present day by virtue of elevated OH-forming reactions with solar wind H ions and a thicker space-weathered rim. Furthermore, the noble gas abundance and microstructural features of components within primitive chondrites that are consistent with palaeo space weathering indicate that many primitive bodies formed from materials that experienced solar wind irradiation during the debris disk stage[65,66]. Many chondrites are breccias, and many asteroids are rubble piles[67], indicating that primitive asteroids may have experienced one, if not several, cycles of accretion, disruption and re-accretion and thus would have incorporated solar-wind-derived water as they re-accreted fine-grained materials that had been exposed to the radiation-rich environment of the early Solar System. Thus, both fine-grained dust, as well as the bodies onto which this dust accreted, contain substantial solar-wind-generated water.

We have modelled the abundance and isotopic composition of water in four reservoirs: enstatite chondrites, water-rich chondrites (CM, CR and CI), ordinary chondrites and solar wind (Methods). If only the average D/H ratio and water abundance of water-rich chondrite and solar wind contributions are considered, the addition of water from solar-wind-irradiated small particles of between 52 and 76% by mass is required alongside water-rich chondrites to produce Earth's D/H ratio (Fig. 4) during the late veneer. However, if only CM meteorites are considered, a 0% contribution by mass of solar-wind-derived water is required (Fig. 4). The water reservoir derived from solar-wind-irradiated fine-grained particles and their calculated mass contribution to Earth during the late veneer is substantially lower than the present day (99% by mass) and the past mass contribution of small particles relative to larger bodies over most of Earth's history[38], but may be consistent with the relative abundance of fine-grained dust and larger planetesimals during the late veneer. In addition, our model predicts that contributions from enstatite chondrites and ordinary chondrites during late-stage accretion of the Earth would reduce the quantity of small solar-wind-irradiated particles required to account for terrestrial D/H ratios. However, the water-poor nature of these chondrites would still necessitate some contribution from fine-grained particles that have been implanted with water by the solar wind for all but the lowest estimate of the water abundance of the bulk Earth (Table 1). In this minimal terrestrial water scenario, no solar-wind-derived water is required but a 94–96% contribution of enstatite or ordinary chondrite-like material is required to provide the low D/H water contribution to Earth's water budget.

Our quantification of the magnitude of water enrichment in solar-wind-irradiated grains implies that the accretion of a reservoir of volatile-rich small particles during the late veneer could reconcile the D/H isotopic composition of Earth's oceans. In addition, the continuous flux of small particles over Earth's history could help to reduce any isotopic fractionation of Earth's oceans by replacing any of the light isotopes of H that could be lost to space over time (for example, ref. [20]).

Methods

Sample preparation. *Itokawa.* Itokawa particle RA-QD02-0279 was mounted on the end of a glass rod with resin (Fig. 1a,b) in the Pb clean lab facility at the Scottish Universities Environmental Research Centre (SUERC). The mounting rod is a typical micro-computed tomography sample mount and was prepared at the Natural History Museum, London, by drilling a hole in the top of a pin and placing a 100-μm-diameter glass rod inside the hole and sealing it with wax. A drop of resin was used to affix the Itokawa grain to the apex of the glass rod to provide access to the majority of the sample's surface. The sample has been stored in contact with the terrestrial atmosphere since it was received from the JAXA Hayabusa Curation facility on 30 June 2017.

SCO. To corroborate the Itokawa APT results a set of pristine and irradiated SCO reference materials were produced.

PSCO. One fragment of PSCO was mounted in resin and polished flat with a water-based polishing suspension. PSCO was dried and exposed to the terrestrial atmosphere in the laboratory for several months.

DSCO. Preparation for irradiation. Saw-cut slices of a single crystal of SCO, 2–3 mm in thickness, were hand polished to 1 μm roughness and diced into pieces approximately 2–3 mm on a side. These SCO pieces were separated into two sets of six sub-samples, set A and set B. Each set was mounted polished-side-up onto a 25 × 25 × 1 mm^3 thick Ta foil (99.9% purity, Goodfellow) using pieces of adhesive carbon conductive tabs (Pelco, Ted Pella) cut to match the size of each sample. The high-atomic-number metal foil and limited extent of the carbon adhesive were chosen to minimize potential sputter cross-contamination of the polished olivine surfaces during irradiation.

Deuterium irradiation of SCO samples. Deuterium irradiation of all DSCO samples was performed using a 10 kV Colutron G-1 ion accelerator at the Sandia National Laboratories Ion Beam Laboratory. Two irradiation experiments were performed at nominally room temperature with D_2^+ ions with energies of 5 keV (for set A) and 1 keV (for set B). The emitted 10 keV and 2 keV D_2^+ ions disassociate on contact with the surface and are implanted as a charged and uncharged D isotope, each with half the energy (5 keV and 1 keV, respectively).

The samples for each irradiation experiment were mounted at once in the ex situ irradiation chamber, which was pumped down to a vacuum of ~10^{-7} torr. No heating or cooling elements were utilized during the experiment, and beam heating was expected to be minimal. The deuterium beam was continuous and focused to about 5 mm, and each sample was irradiated to a fluence of approximately 10^{19} ions per cm^2. The fluence was determined by measuring the current impinging on the stage during the experiment.

DSCO sample transport. Adsorbed and absorbed water is not a major concern because the isotopic signature of deuterium is distinguishable from that of hydrogen. Nevertheless, irradiated surfaces are generally hygroscopic, and we sought to minimize uptake of ambient water vapour during transporting of the samples between University of Hawai'i at Mānoa, Sandia National Laboratories, University of Glasgow and Curtin University. DSCO samples were stored together with a desiccant canister (DriCan, Ted Pella) in a sealed container (Spi-Dry sample preserver, SPI Supplies) back-filled with dry Ar gas before and following deuterium irradiation. Pairs of sub-samples from sets A and B were placed in membrane boxes with a hole in one side and then vacuum packed with desiccant beads for expedited shipping for APT experiments.

HeSCO. Single-crystal olivine was irradiated with 4 keV He^+ under ultra-high-vacuum (UHV) in a specialized surface science instrument (PHI 560; $P = 9 \times 10^{-10}$ torr) at the University of Virginia, as described in previous publications (such as refs. [68,69]). The olivine mineral was cleaved in air before insertion into vacuum and mounted on a copper plate. X-ray photoelectron spectra were taken before and after irradiation at regular fluence intervals, confirming chemical reduction ($Fe^{3+} \rightarrow Fe^{2+} \rightarrow Fe^0$) of iron with simultaneous preferential removal of oxygen and (atmospheric) carbon atoms. Helium ions were generated in an electron-bombardment source at 4 kV and rastered over 6×6 mm^2 for uniform irradiation, providing an average flux of 4.9×10^{13} ions cm^{-2} s^{-1} to a final fluence of 9.2×10^{17} He^+ ions per cm^2. A low-energy electron flood gun was used during irradiation to neutralize surface charge. Samples were then removed from vacuum and stored at atmosphere, before subsequent transport to the NASA Johnson Space Center for analytical electron microscopy and focused ion beam (FIB) sectioning followed by transport to Curtin University.

UHV low-kiloelectronvolt scanning electron imaging. Low-accelerating-voltage SEM surface imaging, including secondary electron images of Itokawa particle RA-QD02-0279, was undertaken to identify mineral phases and space-weathering features such as micrometeorite impact craters (Fig. 1a,b and Extended Data Figs. 1 and 2) to target for subsequent analysis. A low accelerating voltage (5–15 keV) was used to minimize the possibility of mobilizing volatile phases and devolatilizing the space-weathered surfaces of these particles. SEM characterization of particle RA-QD02-0279 was undertaken on the Tescan Mira3, a variable pressure field emission gun (VP-FEG)-SEM at the John de Laeter Centre, Curtin University.

FIB-SEM sample preparation for TEM and APT. All samples were coated with 200 nm of Cr using a Cressington 208HR sputter coater at the John de Laeter Centre, Curtin University. Coating thickness was determined using a crystal thickness monitor and the 200 nm Cr coating was achieved by depositing eight 25 nm layers with a 2 min pause between layers to minimize sample heating. The Cr coating was applied to protect the samples during FIB-SEM sample preparation for APT and TEM, as well as to function as a fiducial marker for the location of the grain surface in FIB-SEM preparation and within the APT datasets. Cr was chosen due to the low concentration of Cr in olivine and because it has a similar ionization potential to silicate phases. Therefore, during APT analysis the voltage and laser energy required to achieve stable field evaporation between these two materials will be similar and will minimize the risk of analysis artefacts and failure.

Several specimens of each sample (Itokawa RA-QD02-0279: front (5, Fig. 1a and Extended Data Fig. 1) and back (5; Fig. 1b, Extended Data Fig. 2); PSCO (5); and DSCO (5)) were prepared for APT using the Tescan Lyra3 dual beam FIB-SEM at the John de Laeter Centre, Curtin University, following the typical lift-out method described in detail in Thompson et al.[70]. One $5 \times 10 \times 0.1$ μm^3 TEM sample was also extracted from Itokawa particle RA-QD02-0279 using the Tescan Lyra3 dual beam FIB-SEM at the John de Laeter Centre, Curtin University. This FIB-SEM uses a mono-isotopic liquid metal ion source of $^{69}Ga^+$ as a high-precision milling beam. In brief, APT specimens were prepared from the region of interest in each sample by depositing a protective layer (2.5×10 μm^2) of Pt, first by electron beam deposition (200 nm thick) and then by ion beam deposition (1 μm). This layer was then undercut using the FIB to produce a wedge 15 μm in length. One end was cut free and attached to a micromanipulator with a Pt weld. The specimen was then cut free from the main mass of the sample and extracted. Prism-shaped segments with 2.5 μm top edges of the wedge were placed, point down, so the space-weathered grain surface of the sample was facing up, onto a pre-grown silica post on a microtip coupon with a Pt deposition and cut free. This process was repeated until all of the wedge had been placed on posts. The samples were then shaped using a progressively smaller annular milling pattern and lower beam current to produce a fine <100-nm-tip-diameter needle-shaped specimen. Care was taken to ensure that all the Pt was milled away but a small amount (~50–100 nm) of Cr remained at the tip of the needle to ensure the preservation of original surface (Extended Data Figs. 1c–h and 2d–h). A final milling process at a 2 kV accelerating voltage was performed to remove approximately the top 20 nm of damaged material produced by the high-energy Ga^+ ion implantation.

TEM methods. The electron-transparent lamella was used for TEM analysis on a FEI Talos FS200X G2 TEM/scanning TEM (STEM) microscope operated at 200 kV and equipped with a Super-X EDS system located in the John de Laeter Centre, Curtin University. Bright-field imaging was used for high-magnification imaging. STEM images and EDS data were captured with a beam current of 0.6 nA. STEM imaging included bright-field, dark-field and HAADF imaging modes. EDS data were collected[71] using FEI Velox software version 2.4.

APT. All APT specimens were analysed on the Cameca Local Electrode Atom Probe (LEAP) 4000X HR Geoscience atom probe, housed at the John de Laeter Centre, Curtin University. The analytical conditions for each run can be found in Extended Data Fig. 7. All analyses were performed in laser-assisted mode using an ultraviolet laser (wavelength $\lambda = 355$ nm). Four samples from Itokawa particle RA-QD02-0279 (two front, shown in Extended Data Fig. 1e,g, (Itokawa1 and Itokawa2) and two back, shown in Extended Data Fig. 2f,h (Itokawa4 and Itokawa3)), one sample from PSCO and three samples from DSCO were run successfully in the APT (Fig. 2 and Extended Data Figs. 3 and 8). These APT samples all initially began field evaporation in the Cr capping layer before passing through any rim feature and into the main material.

The bulk composition of each APT specimen was calculated by measuring the full-width at half-maximum of peaks in the mass-to-charge spectrum (Extended Data Fig. 4). The same range file was used for all APT samples with additional peaks attributed to the DSCO datasets for D, D_2, DO and D_2O. The counting statistical uncertainty for each measured ion peak within the APT datasets was established through the formula below from ref. [72].

$$s = \sqrt{A + B}$$

Where s is the counting statistical uncertainty, A is the total counts beneath a ranged peak including background and B is the average background counts over the same range. These uncertainties were propagated throughout. In all cases, the uncertainties calculated in this way were low (<5%) and had negligible impact on the implications of the study.

Additional sources of uncertainty in APT data that should be considered are derived from detector dead times[73–75]. However, this is only an important consideration when reporting isotope abundances for light elements. As such, it is not accounted for in the present study, which reports only major element and molecular abundances.

Features present in the sample surface, such as chemical profiles, were identified in APT datasets by producing a depth profile using a cylindrical region of interest across the Cr cap and the sample material summing the elemental molecular concentrations over 2 nm bin sizes (Supplementary Data 1). Density fluctuations in the surface of the material were also identified by generating isosurfaces related to the density of ions collected for each element.

The bulk olivine. In all Itokawa APT olivine samples, $^1H^+$ (~1 u Q^{-1}; where u is the unified atomic mass unit, 1 u is 1/12 of the mass of ^{12}C and Q is the charge in Coulombs) steadily increased with depth within the olivine (Fig. 2a–c and Extended Data Fig. 3). This signal was generated by adsorption of residual H on the specimen surface in the UHV chamber and should be considered as noise. This background H level is dependent on a number of factors such as tip shape, the material that is field evaporating, the field around the needle, the temperature and humidity, and so can vary between analyses of the same material[76]. The increase in $^1H^+$ with analysis depth (Fig. 2 and Extended Data Figs. 3 and 8) is commonly observed in APT datasets and is due to the increasing field around the sample generating more H evaporation from the chamber as the radius of the specimen and the voltage increase during analysis. In addition to $^1H^+$, we also observed other water group ions within the mass spectrum such as $^{16}O^1H^+$ (17 u Q^{-1}) $^{16}O^1H_2^+$ (18 u Q^{-1}) $^{16}O^1H_3^+$ (19 u Q^{-1}) (Fig. 2 and Extended Data Figs. 3, 4 and 8) and these peaks were used to quantify the total water content within the APT datasets. This steady enrichment of H was also observed for $^{16}O^1H^+$ (17 u Q^{-1}) (Fig. 2 and Extended Data Figs. 3, 4 and 8) as some of the H within the UHV forms a complex molecular ion with O to produce OH, this trend is also typical for O-bearing APT datasets. The mass peak at 17 u Q^{-1} is predominantly composed of OH. ^{17}O is only 0.04% of the total oxygen[28] and so the contribution of ^{17}O will be below background levels; as such, we assume that the entire 17 u Q^{-1} peak is composed of OH ions. All other ranged ions within the samples remained at a constant level throughout the olivine component of the datasets. As will be discussed later, there was a distinct drop in the abundance of H and hydroxyl ions in all Itokawa APT datasets between 40 and 180 nm (Extended Data Fig. 3) from the olivine grain surface. This drop cannot be generated by a change in the field and is a real property of the H content of the mineral.

The total abundances of H and OH are not constant between APT analysis of the same material, and as such each sample must be corrected separately. The mass peak at 18 u Q^{-1} was a result of the combination of ^{18}O and H_2O ions, ^{18}O was 0.2% of the total oxygen[28] so will have some contribution to the 18 u Q^{-1} peak; in addition some of the H_2O ions will be derived from the combination of ^{16}O with H_2 from the UHV chamber. The mass peak at 18 u Q^{-1} was deconvolved to extract the $^1H_2{}^{16}O^+$ contribution from the $^{18}O^+$ signal assuming a solar $^{16}O/^{18}O$ ratio (ref. [28]) to determine the total contribution form H_2O ions to the 18 u Q^{-1} peak. To calculate the average and maximum total content over the Itokawa samples and the deuterated water content of the DSCO samples, all relevant H (H, H_2, H_3, H_4,

OH, H_2O H_3O) species or D (D, D_2, OD, D_2O) species respectively were ranged using the full width of the peak. To determine the total water component of the bulk olivine, totals for each species (in at%) were calculated by determining the proportion of atoms relative to the total number of atoms under ranged peaks in each dataset extracted from a volume of interest within the bulk olivine material away from any irradiated surface or Cr interface (typically the volume defined by the final 20 nm of the analysis). The sums of the measured at% of all relevant H species were added together to produce mol% totals for water. From these calculations, we could determine that Itokawa olivine APT datasets comprise ~0.5 ± 0.05 mol% water, DSCO comprise ~0.5 ± 0.05 mol% water and PSCO comprise ~0.6 ± 0.05 mol% water. The water abundance in the bulk olivine of Itokawa DSCO and PSCO was substantially higher than the 100–300 parts per million by weight water content measured from bulk olivine in Itokawa grains, LL chondrites and terrestrial olivine[45,51]. This indicates that the majority of the calculated bulk olivine water content in these APT datasets was derived from surface reactions with H_2 in the UHV. This represents a normal UHV contribution of water to the total abundance in each APT sample and allows us to detect deviations from this normal level within the rest of the dataset. To do this, a cylindrical region of interest was generated through each APT data to produce an at% concentration depth profile (Fig. 2, Extended Data Figs. 3, 5 and 8 and Supplementary Data 1) This is an absolute concentration and not a relative abundance as such variations in minor species are not a result of heterogeneity in major species. The data was averaged over 2-nm-thick segments. The average background H (mol%) sum of all H or D species was generated from a summed average of all relevant species from the basal 10 nm of the sample, well within the olivine and away from the irradiated surfaces, as a proxy for the typical APT background. It should be noted that even D species have a nominal background from isobaric interferences with H species. This background water level was subtracted from the water content of each 2 nm segment to generate a real water signal. The average water content was then calculated from the irradiated rims.

Irradiated surfaces. There was no variation within the PSCO for any ion species approaching the olivine grain surface (Extended Data Fig. 8v–x). In particular, the H remained constant within the PSCO olivine grain surface (Extended Data Fig. 8v–x). Within the DSCO and Itokawa APT datasets, the H abundance diminished slightly within the space-weathered or artificially irradiated rims (Fig. 2 and Extended Data Figs. 3 and 8a–n). This depletion of H ions is more pronounced within the DSCO. In addition, OH (17 u Q^{-1}) is also depleted within the DSCO surface (Fig. 2d–j and Extended Data Fig. 8a–n). This enhanced depletion of H in the DSCO was probably caused by the presence of D and corresponding absence of H. Within the DSCO, there is a pronounced 2–3 mol% enrichment in D (2 u Q^{-1}), D_2 (4 u $^{-1}$) DO (18 u Q^{-1}Q) and D_2O (20 u Q^{-1}) in the outermost 40 nm of the grain (Extended Data Figs. 4d and 8a–n). In the Itokawa sample, APT data enrichments in H_2O and OH were observed in the upper 40–60 nm of the sample (Extended Data Figs. 3 and 4a–c). To calculate the total average water content in the space-weathered rim, the sum of the 17, 18 and 19 u Q^{-1} peaks representing $^{17}O^+$+$^1H^{16}O^+$, $^{18}O^+$+$^1H_2{}^{16}O^+$+$^1H^{17}O^+$ and $^1H_3{}^{16}O^+$+$^1H_2{}^{17}O^+$+$^1H^{18}O^+$, respectively, was averaged over the depth of the enrichment, while the total maximum water enrichment was measured from the maximum value detected within the rim. The average water content calculated previously from the bulk olivine was then subtracted from this value to give the total average water, and total maximum water derived from solar wind irradiation. These calculations reveal a maximum total enrichment in water species of 1.6 mol%, 1.4 mol%, 0.24 mol% and 0.7 mol% and an average total enrichment in water species of 0.8 mol%, 0.7 mol%, 0.16 mol% and 0.47 mol% in the upper 50 nm (Extended Data Fig. 1e), 60 nm (Extended Data Fig. 1g), 180 nm (Extended Data Fig. 2f) and 30 nm (Extended Data Fig. 2h) of the grain (Extended Data Fig. 3).

Sputter-coated Cr layer. The H peak decreased substantially in the Cr cap within the DSCO and Itokawa samples but increased within the PSCO APT dataset (Fig. 2 and Extended Data Figs 3 and 8). In the Itokawa and DSCO datasets where more of the Cr cap is preserved, H fluctuates within the cap (Extended Data Figs. 3 and 8a–n). This is probably caused by porosity within the sputter-coated capping layer subtly changing the ionization environment. As such, in all APT datasets the majority of this H signal in the Cr layer is likely to be derived from reactions between H from the UHV system and the Cr layer. In the PSCO, the increase in H in APT data is mirrored by a complementary increase in OH^+ and H_2O^+ ions, suggesting that at least some contribution to these mass peaks is from reactions between H from the UHV system and the Cr layer (Extended Data Fig. 8). In addition, the sputter-coated Cr layer is impure and contains a substantial proportion of O in the form of CrO^+ and CrO^{++} ions (Extended Data Fig. 4a); some of the enrichment in OH^+ and H_2O^+ in the Cr layer is therefore derived from $^{17}O^+$ and $^{18}O^+$ isobaric interferences. This also explains the trend in OH and H_2O abundances in the DSCO and Itokawa APT datasets where OH and H_2O decrease in the Cr layer and then plateau at a lower level than the olivine (Fig. 2 and Extended Data Figs. 3 and 8a–n), revealing the presence of residual O in the Cr layer. Cr metal reacts rapidly when exposed to the terrestrial atmosphere to form CrO and as such the presence of O within the sputter-coated Cr layer is expected. In two DSCO samples (DSCO1 and DSCO3) (Fig. 2d–j and Extended Data Fig. 8a–g,o–u), the Cr cap has a lower concentration of Cr relative to DSCO2, PSCO and Itokawa. This is because these two DSCO samples had a substantially thinner Cr layer remaining after FIB preparation, meaning the APT analysis only briefly measured the Cr layer before transitioning to the DSCO olivine, consequently producing a lower Cr concentration in the Cr capping layer. In the DSCO there is some residual signal from D^+ and D^{2+}, DO^+ D_2O^+ present in the Cr layer; this is due to isobaric interferences with $H_2{}^+$, $H_4{}^+$, $^{18}O^+$ and $^{40}Ca^{++}$ within the sputter-coated Cr capping layer and was observed in all APT samples.

The effect of the Cr–olivine contact. Cr was enriched within the sputter-coated Cr layer as expected. However, in several cases the olivine grain surface was irregular and not normal to the *z* direction of the APT analysis. Thus, the depth profile generated by the wide cylindrical regions of interest in the *z* direction of each APT analysis means that the onset of Cr enrichment and hydrous depletions in the DSCO and Itokawa APT data did not perfectly correlate due to the morphology of the grain surface with respect to the region of interest (Fig. 2 and Extended Data Figs. 3, 5 and 8). Extracting a thinner cylinder for our region-of-interest depth profile revealed that the Cr enrichment and hydrous ion depletions were correlated and related to the compositional change between the sputter-coated Cr and olivine grain surfaces (Extended Data Fig. 5). However, demonstrating this correlation comes at the cost of the counting statistical uncertainty and as such the variations in hydroxide species are less clear (Extended Data Fig. 5). Thus, we chose a cylindrical diameter that acted as a compromise between increasing the amount of data included while preserving the boundary.

In some APT datasets (Itokawa 1, Itokawa 2 and DSCO3) there was a minor enrichment trend in H, OH and H_2O at the boundary between olivine and Cr (Fig. 2 and Extended Data Figs. 3 and 8). This minor enrichment is consistent with the variable H and H_2O contamination on mineral surfaces sometimes observed, and can affect APT datasets to varying degrees[76]. This boundary enrichment in H species was distinct from the secondary enrichment in H species that was found 40 nm beneath the surface of the olivine in Itokawa APT data and in deuterium species in DSCO samples (Fig. 2 and Extended Data Figs. 3 and 8), which we interpret as real H or D implanted by the solar wind or irradiation experiments, respectively.

Grain-size dependence on solar-wind-derived water abundance. The contribution of the solar-wind-derived water to the total water budget of an olivine grain was modelled by varying the space-weathered rim thickness between 10 nm and 200 nm, which are typical depths of space-weathering surfaces[30,45,50], and varying the grain size between 10 nm and 1×10^9 nm. We assumed that the grain was spherical for simplicity, but it should be noted that the resulting water abundance values would be the minimum value for a particle of that size. We calculated the percentage of the volume of each grain that is affected by space weathering and use the APT data to define the minimum water content present within the space-weathered volume to be 1.6 mol%. We then calculated the total water content for the whole grain (Supplementary Data 2). These values were then compared to typical grain sizes for a variety of known extraterrestrial materials to generate Fig. 3.

Earth ocean contribution model. The range of possible water contributions from known Solar System water reservoirs to reconcile Earth's oceans was modelled to determine the possible contributions of water from water-rich chondritic asteroids and solar wind sources that could reproduce Earth's ocean D/H ratio. We assumed the contribution of meteorite-sized objects to be negligible given the bimodal size distribution of objects falling to the Earth[55–58]. We included bulk anyhydrous ordinary chondrites and enstatite chondrites in our model despite the fact that their overall contribution is likely to be small due to their low water content[10,19,77], which is only compatible with the lowest estimate for the water content of the bulk Earth (Table 1); as such, we focused on the aqueously altered water-rich CM, CI and CR chondrites[1,16,78,77]. We assumed a D/H ratio of 1.73×10^{-4} (refs. [1,4]) and water abundance of 2–16 mol% (refs. [78,77]) from water-rich carbonaceous chondrites (an average of CM (D/H 1.48×10^{-4} (refs. [1,16])), CR (D/H 2.57×10^{-4} (ref. [1])) and CI (1.68×10^{-4} (ref. [1],)) based on their current relative abundance in the meteorite collection (CR: 22.3% CM: 76.6% and CI: 1.1%; ref. [79])), an average D/H ratio of 1.31×10^{-4} (refs. [1,4]) and water abundance of 0.1–0.8 mol% for enstatite chondrites, an average D/H ratio of 1.35×10^{-4} (ref. [10]) and water abundance of 0.1–0.7 mol% for ordinary chondrites[19] and a D/H ratio of 2×10^{-7} (refs. [4,26]) and water abundance of 0.1–1.6 mol% for solar-wind-derived water in small particles. The abundance (in mol%) of water-rich chondrites, ordinary chondrites, enstatite chondrites and Earth was converted from the wt% of water in each object (Table 1; 1.6–12.9%, 0.8–0.54% and 0.02%, respectively) using the equation below

$$\mathrm{Water}_{(\mathrm{mol}\%)} = \frac{\left(\frac{\mathrm{Water}_{(\mathrm{wt}\%)} \times A_N}{\mathrm{Mr}_{(H_2O)}}\right) \times 100}{\left[\left(\frac{\mathrm{Water}_{(\mathrm{wt}\%)} \times A_N}{\mathrm{Mr}_{(H_2O)}}\right) + \left(\frac{\left(100 - \mathrm{Water}_{(\mathrm{wt}\%)}\right) \times A_N}{\mathrm{M}_{(\mathrm{bulk})}}\right)\right]}$$

Where A_N is Avogadro's constant (6.022×10^{23}), $\mathrm{Mr}_{(H2O)}$ is the molecular mass of water (18 g mol^{-1}), $\mathrm{Mr}_{(\mathrm{bulk})}$ is the average molecular mass of the body in question

without water (21.2 g mol^{-1} for the bulk silicate Earth[80], 24 g mol^{-1} for carbonaceous chondrites[81], 25.6 g mol^{-1} for enstatite chondrites and 24.4 g mol^{-1} was used for ordinary chondrites[81]). We modelled the mixture of each of these reservoirs and our newly defined water budget of space-weathered fine-grained particles. By allowing the mass proportion of each reservoir to vary, we calculated solutions for this two-component model for each Solar System water source using the equation below.

$$\mathrm{D/H}_{(\mathrm{average})} = \left[\frac{\left(\mathrm{Mass\ fraction}_{\mathrm{SW}} \times \mathrm{SW}_{\mathrm{water}_{(\mathrm{mol}\%)}} \times \mathrm{D/H}_{\mathrm{SW}}\right) + \left((1 - \mathrm{Mass\ fraction}_{\mathrm{SW}}) \times \mathrm{Asteroid}_{\mathrm{water}_{(\mathrm{mol}\%)}} \times \mathrm{D/H}_{\mathrm{Asteroid}}\right)}{\left(\mathrm{Mass\ fraction}_{\mathrm{SW}} \times \mathrm{SW}_{\mathrm{water}_{(\mathrm{mol}\%)}}\right) + \left((1 - \mathrm{Mass\ fraction}_{\mathrm{SW}}) \times \mathrm{Asteroid}_{\mathrm{water}_{(\mathrm{mol}\%)}}\right)}\right]$$

This allowed us to determine mass proportions of each material relative to fine-grained solar-wind-irradiated particles that can reproduce the present-day SMOW D/H ratio of 1.557×10^{-4} and the bulk Earth D/H of 1.49×10^{-4} of the Earth[1,17] (Supplementary Data 3).

Our model is consistent for the assumptions outlined above; however, it should be noted that a recent study from Vacher et al.[82], showed that water-rich chondrites may have adsorbed substantial amounts of water from the terrestrial atmosphere. This would serve to increase on average the D/H ratio of water-rich chondrites[82], which would, in turn, increase the contribution of fine-grained solar-wind-irradiated particulates required. In addition, the total mol% water of water-rich chondrites would be lower once terrestrial adsorbed water was removed[82], which would serve to reduce the contribution of fine-grained solar-wind-irradiated particles required. However, the amended water abundance values of Vacher et al.[82], are within the range of our current model.

In addition, if we consider only the contribution of <10 µm fine-grained solar-wind-irradiated particles that would be sufficiently water-rich (Fig. 3) and represent 1–10% by mass of the total amount of fine-grained extraterrestrial material incident on the Earth today[58], then this would require a larger total contribution of fine-grained materials of up to 90–94% of the final 0.5 ± 0.25% of Earth's mass during the late veneer (Extended Data Fig. 6). While this greater contribution by mass of fine-grained particles is consistent with the contribution of fine-grained particles to the mass flux of extraterrestrial materials incident on the Earth throughout its history[38], it is unlikely to be the case that the debris disk was sufficiently dust rich. However, if the particle size distribution of fine-grained materials during the late veneer was more fine-grained than that of the present day, with a greater proportion by mass of <10 µm particles, this would serve to reduce the required fine-grained contribution. An increased abundance of fine-grained <10 µm grains in the inner Solar System is consistent with numerical simulations of IDP grain-size variation and distribution that predict a high proportion of ~5 µm particles in the inner Solar System region[42]. In addition, the coarser component of dust particles >10 µm typically composed of fine-grained porous aggregates (such as IDPs and fragments of chondritic matrix) would contain substantially more solar-wind-derived water than predicted by our spherical grain model (Fig. 3) and would be comparable in water content to the <10 µm grains. This would also serve to reduce the contribution by mass of fine-grained dust during the late veneer.

The contribution of solar-wind-derived water may not be limited to delivery from fine-grained dust, as during the debris disk stage all materials will experience a radiation-rich environment. Thus, all dust produced during this period will incorporate solar-wind-derived water. Much of this irradiated material will re-accrete onto and/or form primitive asteroids. Consequently, solar-wind-derived water will be incorporated into the regolith of primitive asteroids as this dust is re-accreted, while many primitive asteroids probably formed from the re-accretion of fine-grained space-weathered materials. Therefore, both water-rich fine-grained dust and water-rich asteroids/asteroid regoliths derived from the (re)accretion of this water-rich dust will be produced in the early Solar System. This is consistent with evidence of space weathering and solar wind irradiation of, and incorporation into, chondritic regolith breccias[65,66] and the prevalence of rubble pile asteroids[67].

Samples. The Itokawa particles are on loan to L.D. from JAXA as part of the 5th International Announcement of Opportunity. At present they are stored at the University of Glasgow and any remaining fragments and samples will be returned to JAXA on the completion of the project. Because of the nature of APT measurements, all atom probe samples detailed in this study have been destroyed. The SCO reference materials produced for this study are stored at Curtin University (PSCO), University of Hawaii (DSCO) and JSC (HeSCO).

Data availability

All data generated or analysed during this study are either included in the Article and its Supplementary Information or are available at the following open-access data repository https://doi.org/10.5525/gla.researchdata.1164. The open access data repository also contains all source data.

Received: 9 November 2020; Accepted: 10 August 2021;
Published online: 29 November 2021

References

1. Alexander, C. M. O. D. The origin of inner Solar System water. *Phil. Trans. R. Soc.* **375**, 20150384 (2017).
2. Marty, B. The origins and concentrations of water, carbon, nitrogen and noble gases on Earth. *Earth Planet. Sci. Lett.* **313**, 56–66 (2012).
3. Meech, K. & Raymond, S. N. in *Planetary Astrobiology* (eds Meadows V. et al.) 325–353 (Univ. of Arizona, Tuscon, 2020).
4. Robert, F. The origin of water on Earth. *Science* **293**, 1056–1058 (2001).
5. Greenwood, J. P. et al. Hydrogen isotope ratios in lunar rocks indicate delivery of cometary water to the Moon. *Nat. Geosci.* **4**, 79–82 (2011).
6. Hallis, L. J. et al. Evidence for primordial water in Earth's deep mantle. *Science* **350**, 795–797 (2015).
7. Ikoma, M. & Genda, H. Constraints on the mass of a habitable planet with water of nebular origin. *Astrophys. J.* **648**, 696 (2006).
8. Morbidelli, A. et al. Fossilized condensation lines in the Solar System protoplanetary disk. *Icarus* **267**, 368–376 (2016).
9. Morbidelli, A. et al. Source regions and timescales for the delivery of water to the Earth. *Meteor. Planet. Sci.* **35**, 1309–1320 (2000).
10. Piani, L. et al. Earth's water may have been inherited from material similar to enstatite chondrite meteorites. *Science* **369**, 1110–1113 (2020).
11. O'Brien, D. P., Walsh, K. J., Morbidelli, A., Raymond, S. N. & Mandell, A. M. Water delivery and giant impacts in the 'Grand Tack' scenario. *Icarus* **239**, 74–84 (2014).
12. Raymond, S. N. & Izidoro, A. The empty primordial asteroid belt. *Sci. Adv.* **3**, e1701138 (2017).
13. Raymond, S. N., Quinn, T. & Lunine, J. I. High-resolution simulations of the final assembly of Earth-like planets I. Terrestrial accretion and dynamics. *Icarus* **183**, 265–282 (2006).
14. Walsh, K. J., Morbidelli, A., Raymond, S. N., O'Brien, D. P. & Mandell, A. M. A low mass for Mars from Jupiter's early gas-driven migration. *Nature* **475**, 206–209 (2011).
15. Bates, H., King, A., Donaldson Hanna, K., Bowles, N. & Russell, S. Linking mineralogy and spectroscopy of highly aqueously altered CM and CI carbonaceous chondrites in preparation for primitive asteroid sample return. *Meteor. Planet. Sci.* **55**, 77–101 (2020).
16. McCubbin, F. M. & Barnes, J. J. Origin and abundances of H_2O in the terrestrial planets, Moon, and asteroids. *Earth Planet. Sci. Lett.* **526**, 115771 (2019).
17. Lécuyer, C., Gillet, P. & Robert, F. The hydrogen isotope composition of seawater and the global water cycle. *Chem. Geol.* **145**, 249–261 (1998).
18. Marty, B. et al. Origins of volatile elements (H, C, N, noble gases) on Earth and Mars in light of recent results from the ROSETTA cometary mission. *Earth Planet. Sci. Lett.* **441**, 91–102 (2016).
19. Jin, Z. & Bose, M. New clues to ancient water on Itokawa. *Sci. Adv.* **5**, eaav8106 (2019).
20. Genda, H. & Ikoma, M. Origin of the ocean on the Earth: early evolution of water D/H in a hydrogen-rich atmosphere. *Icarus* **194**, 42–52 (2008).
21. Asaduzzaman, A., Muralidharan, K. & Ganguly, J. Incorporation of water into olivine during nebular condensation: insights from density functional theory and thermodynamics, and implications for phyllosilicate formation and terrestrial water inventory. *Meteor. Planet. Sci.* **50**, 578–589 (2015).
22. Sasaki, S. The primary solar-type atmosphere surrounding the accreting Earth: H_2O-induced high surface temperature. In *LPI Conference on the Origin of the Earth* (eds Newsom, H. E. & Jones, J. H.) 195–209 (SAO, NASA Astrophysics Data System, 1990).
23. Dauphas, N. & Marty, B. Inference on the nature and the mass of Earth's late veneer from noble metals and gases. *J. Geophys. Res. Planets* **107**, E12, 12-1 (2002).
24. Day, J. M., Pearson, D. G. & Taylor, L. A. Highly siderophile element constraints on accretion and differentiation of the Earth-Moon system. *Science* **315**, 217–219 (2007).
25. Walker, R. J. Highly siderophile elements in the Earth, Moon and Mars: update and implications for planetary accretion and differentiation. *Geochemistry* **69**, 101–125 (2009).
26. Huss, G., Nagashima, K., Burnett, D., Jurewicz, A. & Olinger, C. A new upper limit on the D/H ratio in the solar wind. *LPI* 1709 (2012).
27. Geiss, J. & Gloeckler, G. in *Primordial Nuclei and their Galactic Evolution* (eds von Steiger, R. et al.) 239–250 (Springer, 1998).
28. Lodders, K. Solar system abundances and condensation temperatures of the elements. *Astrophys. J.* **591**, 1220 (2003).
29. Marty, B., Chaussidon, M., Wiens, R., Jurewicz, A. & Burnett, D. A ^{15}N-poor isotopic composition for the solar system as shown by Genesis solar wind samples. *Science* **332**, 1533–1536 (2011).
30. Bradley, J. P. et al. Detection of solar wind-produced water in irradiated rims on silicate minerals. *Proc. Natl Acad. Sci. USA* **111**, 1732–1735 (2014).
31. Ichimura, A., Zent, A., Quinn, R., Sanchez, M. & Taylor, L. Hydroxyl (OH) production on airless planetary bodies: evidence from H+/D+ ion-beam experiments. *Earth Planet. Sci. Lett.* **345**, 90–94 (2012).

32. Liu, Y. et al. Direct measurement of hydroxyl in the lunar regolith and the origin of lunar surface water. *Nat. Geosci.* **5**, 779–782 (2012).
33. Lucey, P. et al. Understanding the lunar surface and space-Moon interactions. *Rev. Min. Geochem.* **60**, 83–219 (2006).
34. Zhu, C. et al. Untangling the formation and liberation of water in the lunar regolith. *Proc. Natl Acad. Sci. USA* **116**, 11165–11170 (2019).
35. Bandfield, J. L., Poston, M. J., Klima, R. L. & Edwards, C. S. Widespread distribution of OH/H_2O on the lunar surface inferred from spectral data. *Nat. Geosci.* **11**, 173–177 (2018).
36. Pieters, C. M. et al. Character and spatial distribution of OH/H_2O on the surface of the Moon seen by M3 on Chandrayaan-1. *Science* **326**, 568–572 (2009).
37. Sunshine, J. M. et al. Temporal and spatial variability of lunar hydration as observed by the Deep Impact spacecraft. *Science* **326**, 565–568 (2009).
38. Pasek, M. & Lauretta, D. Extraterrestrial flux of potentially prebiotic C, N, and P to the early Earth. *Origins Life Evol. Biosph.* **38**, 5–21 (2008).
39. Canup, R. M. Simulations of a late lunar-forming impact. *Icarus* **168**, 433–456 (2004).
40. Krot, A. N., Amelin, Y., Cassen, P. & Meibom, A. Young chondrules in CB chondrites from a giant impact in the early Solar System. *Nature* **436**, 989–992 (2005).
41. MacGregor, M. A. et al. Constraints on planetesimal collision models in debris disks. *Astrophys. J.* **823**, 79 (2016).
42. Poppe, A. R. An improved model for interplanetary dust fluxes in the outer Solar System. *Icarus* **264**, 369–386 (2016).
43. Reddy, S. M. et al. Atom probe tomography: development and application to the geosciences. *Geostand. Geoanal. Res.* **44**, 5–50 (2020).
44. Nakamura, T. et al. Itokawa dust particles: a direct link between S-type asteroids and ordinary chondrites. *Science* **333**, 1113–1116 (2011).
45. Noguchi, T. et al. Incipient space weathering observed on the surface of Itokawa dust particles. *Science* **333**, 1121–1125 (2011).
46. Greer, J. et al. Atom probe tomography of space-weathered lunar ilmenite grain surfaces. *Meteor. Planet. Sci.* **55**, 426–440 (2020).
47. Noguchi, T. et al. Space weathered rims found on the surfaces of the Itokawa dust particles. *Meteor. Planet. Sci.* **49**, 188–214 (2014).
48. Nagao, K. et al. Irradiation history of Itokawa regolith material deduced from noble gases in the Hayabusa samples. *Science* **333**, 1128–1131 (2011).
49. Crider, D. H. & Vondrak, R. Hydrogen migration to the lunar poles by solar wind bombardment of the Moon. *Adv. Space Res.* **30**, 1869–1874 (2002).
50. Keller, L. P. & McKay, D. S. The nature and origin of rims on lunar soil grains. *Geochim. Cosmochim. Acta* **61**, 2331–2341 (1997).
51. Demouchy, S., Jacobsen, S. D., Gaillard, F. & Stern, C. R. Rapid magma ascent recorded by water diffusion profiles in mantle olivine. *Geology* **34**, 429–432 (2006).
52. Nuth, J. A. III, Brearley, A. J. & Scott, E. R. in *Chondrites and the Protoplanetary Disk* (eds Krot, A.N. et al.) Vol. 341, 675 (Annual Reviews, 2005).
53. Bland, P. A. et al. Why aqueous alteration in asteroids was isochemical: high porosity ≠ high permeability. *Earth Planet. Sci. Lett.* **287**, 559–568 (2009).
54. Rietmeijer, F. J. Size distributions in two porous chondritic micrometeorites. *Earth Planet. Sci. Lett.* **117**, 609–617 (1993).
55. Zolensky, M. E. et al. Mineralogy and petrology of comet 81 P/Wild 2 nucleus samples. *Science* **314**, 1735–1739 (2006).
56. Love, S. & Brownlee, D. A direct measurement of the terrestrial mass accretion rate of cosmic dust. *Science* **262**, 550–553 (1993).
57. Anders, E. Pre-biotic organic matter from comets and asteroids. *Nature* **342**, 255–257 (1989).
58. Flynn, G., Keller, L., Jacobsen, C. & Wirick, S. An assessment of the amount and types of organic matter contributed to the Earth by interplanetary dust. *Adv. Space Res.* **33**, 57–66 (2004).
59. Ishii, H. A. et al. Multiple generations of grain aggregation in different environments preceded solar system body formation. *Proc. Natl Acad. Sci. USA* **115**, 6608–6613 (2018).
60. Vican, L. & Schneider, A. The evolution of dusty Debris disks around solar type stars. *Astrophys. J.* **780**, 154 (2013).
61. Wyatt, M. The insignificance of PR drag in detectable extrasolar planetesimal belts. *Astron. Astrophys.* **433**, 1007–1012 (2005).
62. Nesvorný, D. et al. Cometary origin of the zodiacal cloud and carbonaceous micrometeorites. Implications for hot debris disks. *Astrophys. J.* **713**, 816 (2010).
63. Ayres, T. R. Evolution of the solar ionizing flux. *J. Geophys. Res. Planets* **102**, 1641–1651 (1997).
64. Kass, D. & Yung, Y. L. Loss of atmosphere from Mars due to solar wind-induced sputtering. *Science* **268**, 697–699 (1995).
65. Suess, H., Wänke, H. & Wlotzka, F. On the origin of gas-rich meteorites. *Geochim. Cosmochim. Acta* **28**, 595–607 (1964).
66. Krietsch, D. et al. Noble gases in CM carbonaceous chondrites: effect of parent body aqueous and thermal alteration and cosmic ray exposure ages. *Geochim. Cosmochim. Acta.* **310**, 240–280 (2021).
67. Walsh, K. J. Rubble pile asteroids. *Annu. Rev. Astron. Astrophys.* **56**, 593–624 (2018).
68. Dukes, C., Baragiola, R. & McFadden, L. Surface modification of olivine by H^+ and He+ bombardment. *J. Geophys. Res. Planets* **104**, 1865–1872 (1999).
69. Loeffler, M., Dukes, C. & Baragiola, R. Irradiation of olivine by 4 keV He^+: Simulation of space weathering by the solar wind. *J. Geophys. Res. Planets* **114**, E3 (2009).
70. Thompson, K. et al. In situ site-specific specimen preparation for atom probe tomography. *Ultramicroscopy* **107**, 131–139 (2007).
71. MacArthur, K. E. et al. Optimizing experimental conditions for accurate quantitative energy-dispersive X-ray analysis of interfaces at the atomic scale.*Microscopy Microanalysis* **27**, 1–15 (2021).
72. Larson, D. J., Prosa, T., Ulfig, R. M., Geiser, B. P. & Kelly, T. F. *Local Electrode Atom Probe Tomography* Vol. 2 (Springer Science, 2013).
73. Lewis, J. B., Isheim, D., Floss, C. & Seidman, D. N. C^{12}/C^{13}-ratio determination in nanodiamonds by atom-probe tomography. *Ultramicroscopy* **159**, 248–254 (2015).
74. Meisenkothen, F., Steel, E. B., Prosa, T. J., Henry, K. T. & Kolli, R. P. Effects of detector dead-time on quantitative analyses involving boron and multi-hit detection events in atom probe tomography. *Ultramicroscopy* **159**, 101–111 (2015).
75. Stephan, T., Heck, P. R., Isheim, D. & Lewis, J. B. Correction of dead time effects in laser-induced desorption time-of-flight mass spectrometry: applications in atom probe tomography. *Int. J. Mass Spectrom.* **379**, 46–51 (2015).
76. Kolli, R. P. Controlling residual hydrogen gas in mass spectra during pulsed laser atom probe tomography. *Adv. Struct. Chem. Imag.* **3**, 1–10 (2017).
77. Alexander, C. M. D., McKeegan, K. D. & Altwegg, K. Water reservoirs in small planetary bodies: meteorites, asteroids, and comets. *Space Sci. Rev.* **214**, 1–47 (2018).
78. Garenne, A. et al. The abundance and stability of "water" in type 1 and 2 carbonaceous chondrites (CI, CM and CR). *Geochim. Cosmochim. Acta* **137**, 93–112 (2014).
79. LPI. *The Meteoritical Bulletin* (The Meteoritical Society, 2020); https://www.lpi.usra.edu/meteor/metbull.php
80. Szurgot M. Mean atomic weight of Earth, Moon, Venus, Mercury and Mars. Effect of mass of cores and density of planets. In *46th Lunar and Planetary Science Conference* 1536 (USRA, 2015); https://www.hou.usra.edu/meetings/lpsc2015/pdf/1536.pdf
81. Anderson, D. L. & Kovach, R. L. The composition of the terrestrial planets. *Earth Planet. Sci. Lett.* **3**, 19–24 (1967).
82. Vacher, L. G. et al. Hydrogen in chondrites: influence of parent body alteration and atmospheric contamination on primordial components. *Geochim. Cosmochim. Acta* **281**, 53–66 (2020).
83. Greenberg, J. M. Making a comet nucleus. *Astron. Astrophys.* **330**, 375–380 (1998).
84. Peslier, A. H., Schönbächler, M., Busemann, H. & Karato, S.-I. Water in the Earth's interior: distribution and origin. *Space Sci. Rev.* **212**, 743–810 (2017).

Acknowledgements

The Hayabusa-returned sample RA-QD02-0279 was allocated to L.D. by the Planetary Material Sample Curation Facility of JAXA through the 5th International Announcement of Opportunity held in 2017. We would like to thank M. Suttle for the preparation and loan of the mounting rod, R. Ickert for providing access to the clean lab facility at the Scottish Universities Environmental Research Centre to mount the Itokawa particles and R. Mahajan for providing suitably fine-grained basaltic fragments to practice on. L.D. would also like to thank NASA JSC and the Lunar and Planetary Institute for the training received at the 4th training in extraterrestrial sample handling course. This work was funded by the UK STFC consortium grant numbers ST/T002328/1 awarded to M.R.L. and L.D. and ST/N000846/1 awarded to M.R.L. This work was also funded by a UAE seed grant awarded to M.R.L., as well as a SAGES small grant awarded to L.D. H.I. and J.P.B. were partially supported by the NASA Laboratory Analysis of Returned Samples (LARS) Program (grant number 80NSSC18K0936). This work was partially supported through the INL Laboratory Directed Research & Development (LDRD) Program under DOE Idaho Operations Office contract number DE-AC07-05ID145142, which supported J.A.A. D.F. is supported by an Australian Research Council Discovery Early Career Reseacher Award (ARC DECRA) number DE190101307. This work was conducted within the Geoscience Atom Probe Facility at Curtin University, which was developed through funding from the Science and Industry Endowment Fund (grant number SIEF RI13-01) awarded to S.M.R. This work utilized the Tescan MIRA3 FE-SEM at the John de Laeter Centre, Curtin University, which was obtained via funding from the Australian Research Council LIEF program (grant number ARC LE130100053). We acknowledge the use of Curtin University's Microscopy and Microanalysis Facility, whose instrumentation has been partially funded by the University, State and Commonwealth Governments. This work was performed, in part, at the Center for Integrated Nanotechnologies, an Office of Science User Facility operated for the US DOE Office of Science. Sandia National Laboratories is a multi-mission laboratory managed and operated by National Technology and Engineering Solutions of Sandia, LLC, a wholly owned subsidiary of Honeywell International, Inc., for the US DOE's National Nuclear Security Administration under

contract number DE-NA-0003525. The views expressed in the article do not necessarily represent the views of the US DOE or the United States Government.

Author contributions

L.D. conceived the project with input from M.R.L. Itokawa sample handling and mounting was conducted by M.A.C. and L.D. Itokawa SEM analysis was conducted by T.S., M.A.C. and L.D. H.A.I. and J.P.B. prepared the polished SC olivine on Ta for D_2^+ irradiation. J.A.A. arranged and advised on instrumentation for D_2^+ irradiation. K.H. and A.M. performed D_2^+ irradiations. L.P.K., R.C. and M.S.T. prepared the polished SC olivine for He^+ irradiation and C.A.D. and M.J.L. conducted the irradiation. L.D. and S.M.R. prepared the polished SC olivine and conducted the laboratory exposure. Cr coating was undertaken by W.D.A.R., D.F. and L.D. FIB preparations for TEM and APT were undertaken by L.D., D.F. and W.D.A.R. TEM work was conducted by Z.Q., L.D. and W.D.A.R. APT analysis was undertaken by D.W.S., D.F. and L.D. The results were interpreted by L.D., P.A.B., L.V.F., M.R.L., L.J.H., N.E.T., F.J., D.W.S., D.F. and E.C. L.D., H.I. and W.D.A.R. wrote the methods. L.D. wrote the paper with input from all co-authors.

Competing interests

The authors declare no competing interests.

Additional information

Extended data is available for this paper at https://doi.org/10.1038/s41550-021-01487-w.

Supplementary information The online version contains supplementary material available at https://doi.org/10.1038/s41550-021-01487-w.

Correspondence and requests for materials should be addressed to Luke Daly.

Peer review information *Nature Astronomy* thanks Sean Raymond and the other, anonymous, reviewer(s) for their contribution to the peer review of this work.

Reprints and permissions information is available at www.nature.com/reprints.

Publisher's note Springer Nature remains neutral with regard to jurisdictional claims in published maps and institutional affiliations.

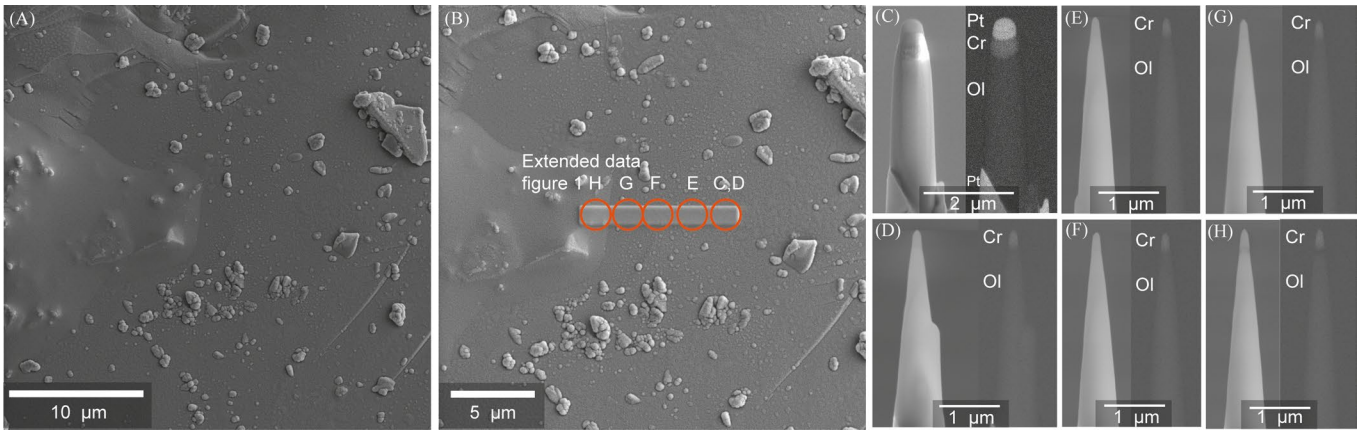

Extended Data Fig. 1 | Back scatter electron (BSE) and in-beam secondary electron (IbSE) images of the front face of Itokawa particle RA-QD02-0279 and resulting APT specimens. a, BSE image of the front face of Itokawa particle RA-QD02-0279 after Cr coating. **b**, BSE image of the front face of Itokawa particle RA-QD02-0279 after Ion beam Pt deposition in preparation for sample extraction for APT. The red circles indicate where the APT lift outs were extracted from the wedge. **C**) IbSE (left) and BSE (right) image of needle (**D**) half way through annular milling. The Pt protective layer is visible as well as the Cr layer. Annular milling was continued until the Pt was removed but leaving the Cr cap. **D**–**H**) IbSE (left) and BSE images (right) of each APT needle the Cr cap is visible at the apex of each tip in the BSE images as well as the Pt weld at the base.

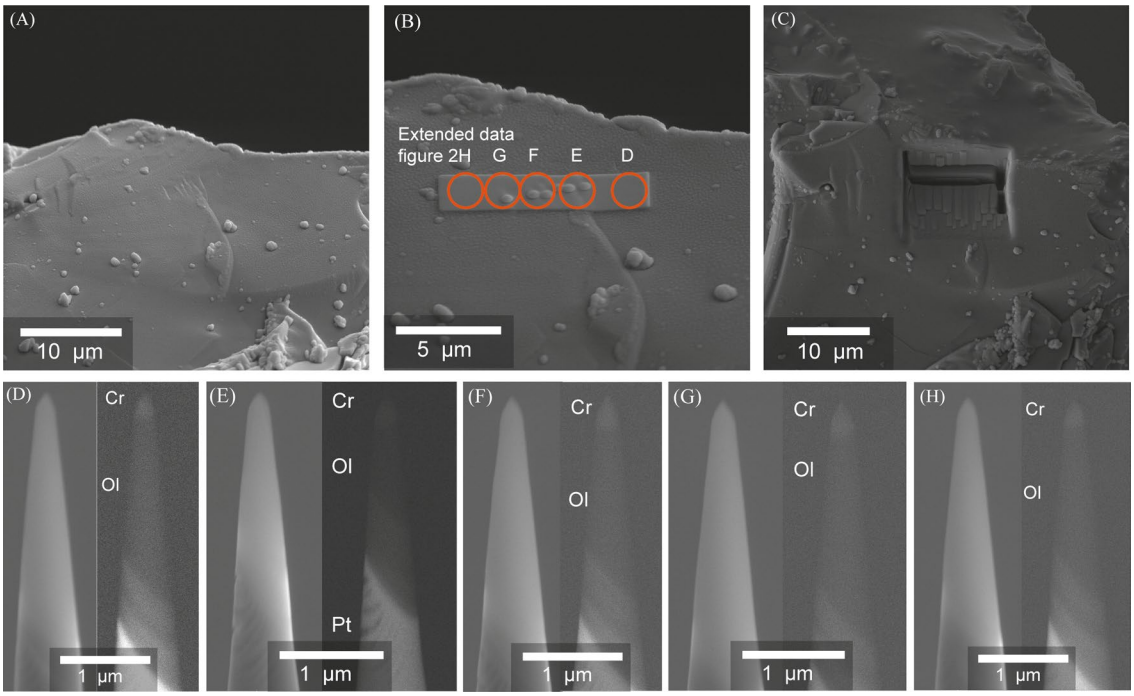

Extended Data Fig. 2 | Back scatter electron (BSE) and in-beam secondary electron (IbSE) images of the back face of Itokawa particle RA-QD02-0279 and resulting APT specimens. a, BSE image of the back face of Itokawa particle RA-QD02-0279 after Cr coating. **b**, BSE image of the back face of Itokawa particle RA-QD02-0279 after Ion beam Pt deposition in preparation for sample extraction for APT. The red circles indicate where the APT lift outs were extracted from the wedge. **c**, BSE image of the back face of Itokawa particle RA-QD02-0279 after FIB lift out. **D**–**H**) IbSE (left) and BSE images (right) of each APT needle the Cr cap is visible at the apex of each tip in the BSE images as well as the Pt weld at the base.

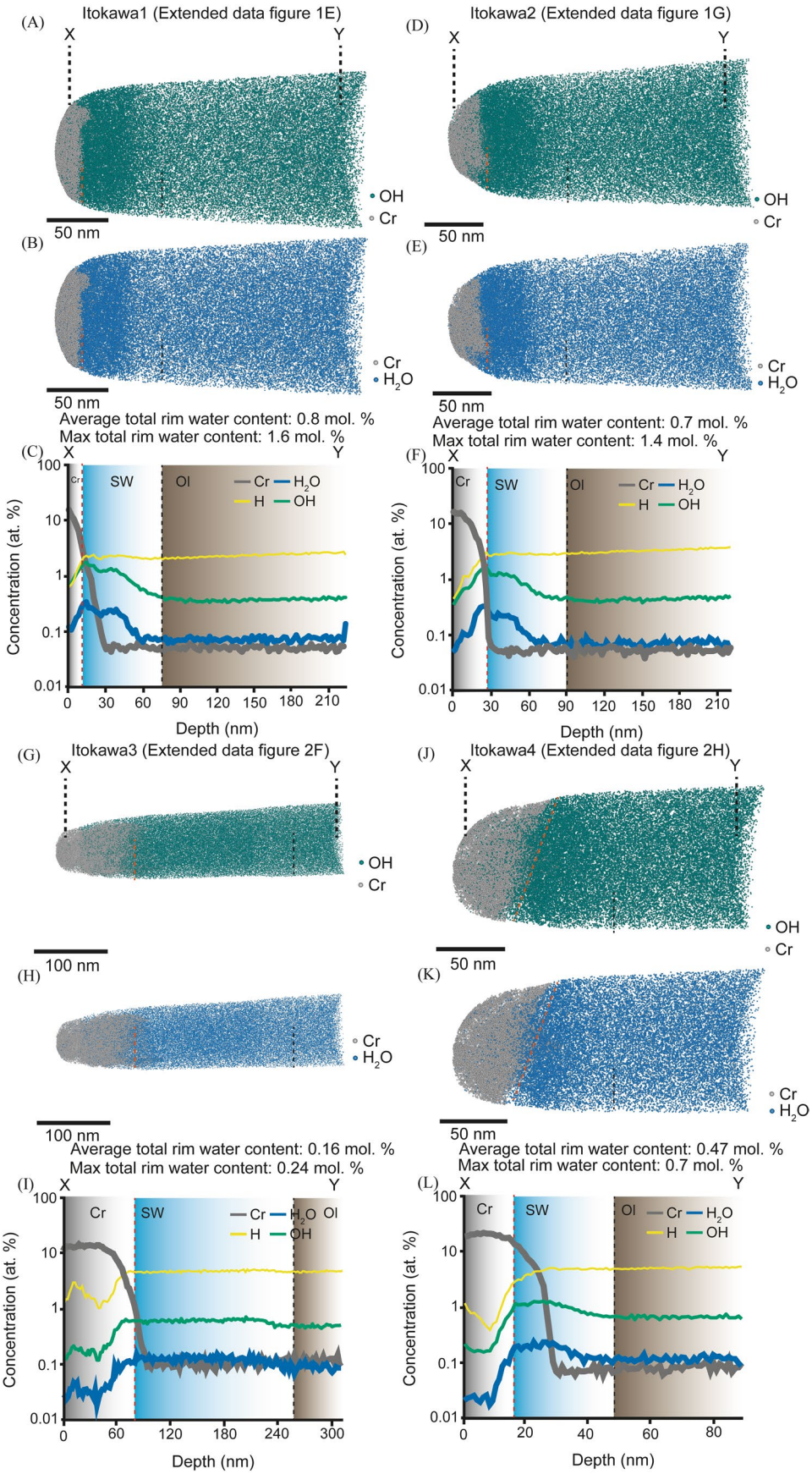

Extended Data Fig. 3 | See next page for caption.

Extended Data Fig. 3 | APT data from Itoakwa particle RA_QD02_0279. The APT needles extracted from the front face of Itokawa particle RA_QD02_0279 shown in Extended Data Fig. 1E (**A**–**C**) and Extended Data Fig. 1G (**D**–**F**) and from the back face shown in Extended Data Fig. 2F (**G**–**I**) and Extended Data Fig. 2H (**J**–**L**). All data extend from the Cr protective layer (grey spheres) through RA_QD02_0279's space weathered surface into unweathered olivine. (**A**, **D**, **G**, and **J**) APT measurement of the 3D distribution of Cr (grey spheres) and OH (teal spheres). (**B**, **E**, **H**, and **K**) APT measurement of the 3D distribution of Cr (grey spheres) and H_2O (blue spheres) ions. (**C**, **F**, **I**, and **L**) Concentration of ions in atomic percent (at. %) with depth across the Cr capping layer (Cr, grey shaded region) space weathered rim (SW, blue shaded region) and the non-space weathered olivine (Ol, brown shaded region) revealing variations in the abundances of Cr (grey line), H (yellow line), OH (green line) and H_2O (blue line) ions. Line widths have been adjusted to represent the 1 sigma uncertainty and depth profiles are absolute abundances not relative concentrations (Supplementary Data 1). The boundary between the Cr and SW layer is marked by a vertical dashed red line and the boundary between the SW and Ol layer is marked by a vertical black dashed line.

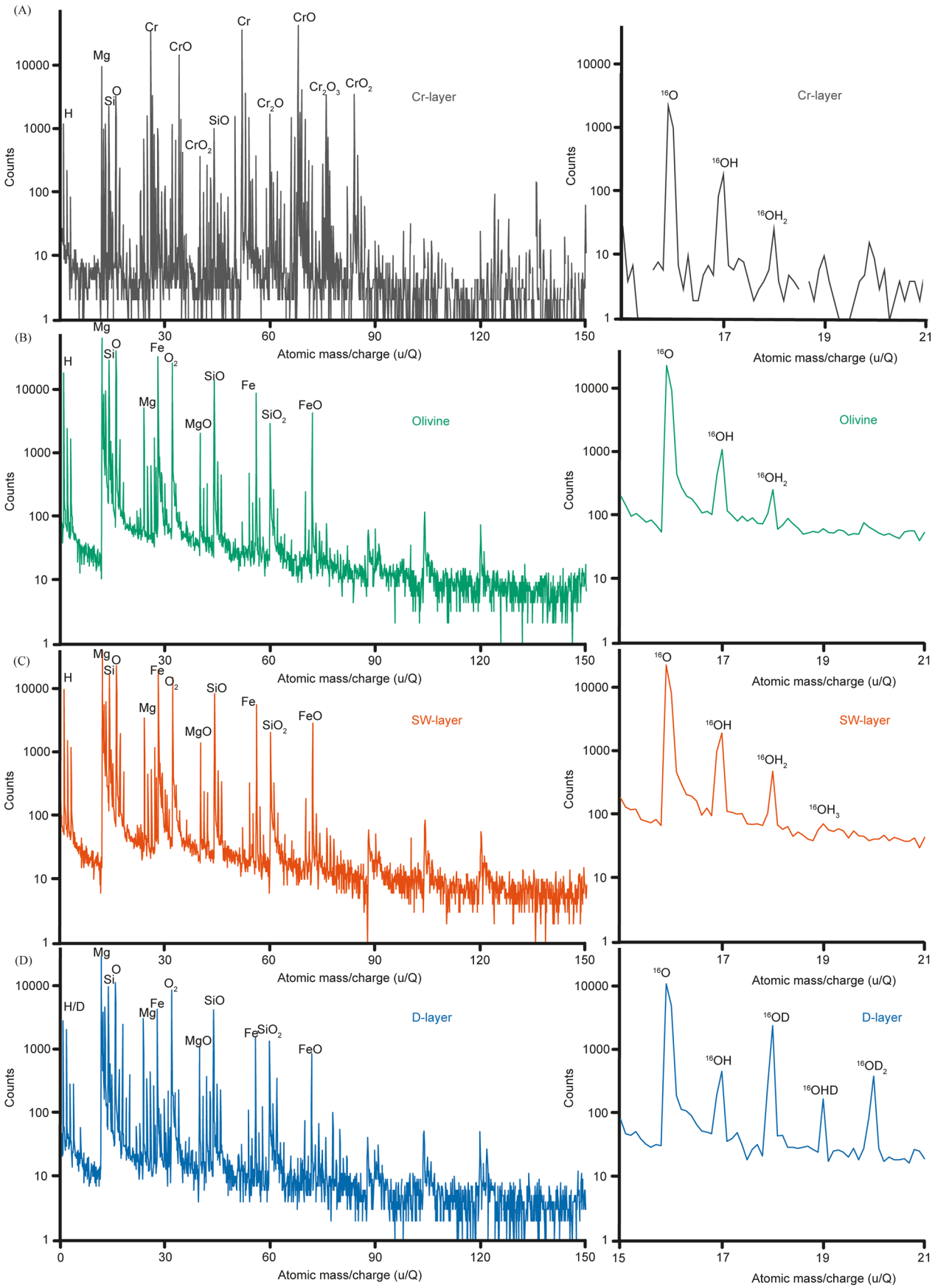

Extended Data Fig. 4 | See next page for caption.

Extended Data Fig. 4 | Representative full APT mass to charge state spectra and localized mass to charge state spectra highlighting the oxygen series mass to charge peaks. Mass to charge state (Atomic mass/charge (u/Q)) spectra showing the histogram of the number of ion counts detected at each u/Q step. For each the mass-to charge state ratio spectra the detected ions were produced from regions of interest within: **A**) the sputter coated Cr layer from Extended Data Fig. 3J-L, **B**) the bulk olivine of Itokawa from Extended Data Fig. 3J-L, **C**) the solar wind irradiated rim of Itokawa olivine from Extended Data Fig. 3J-L, **D**) D-irradiated rim from Extended Data Figure 8H-N. (**A**–**D**) show the entire mass to charge state spectra from 0-150 u/Q. (E-H) show the APT mass to charge state between 16-21 u/Q that contains the Oxygen series peaks.

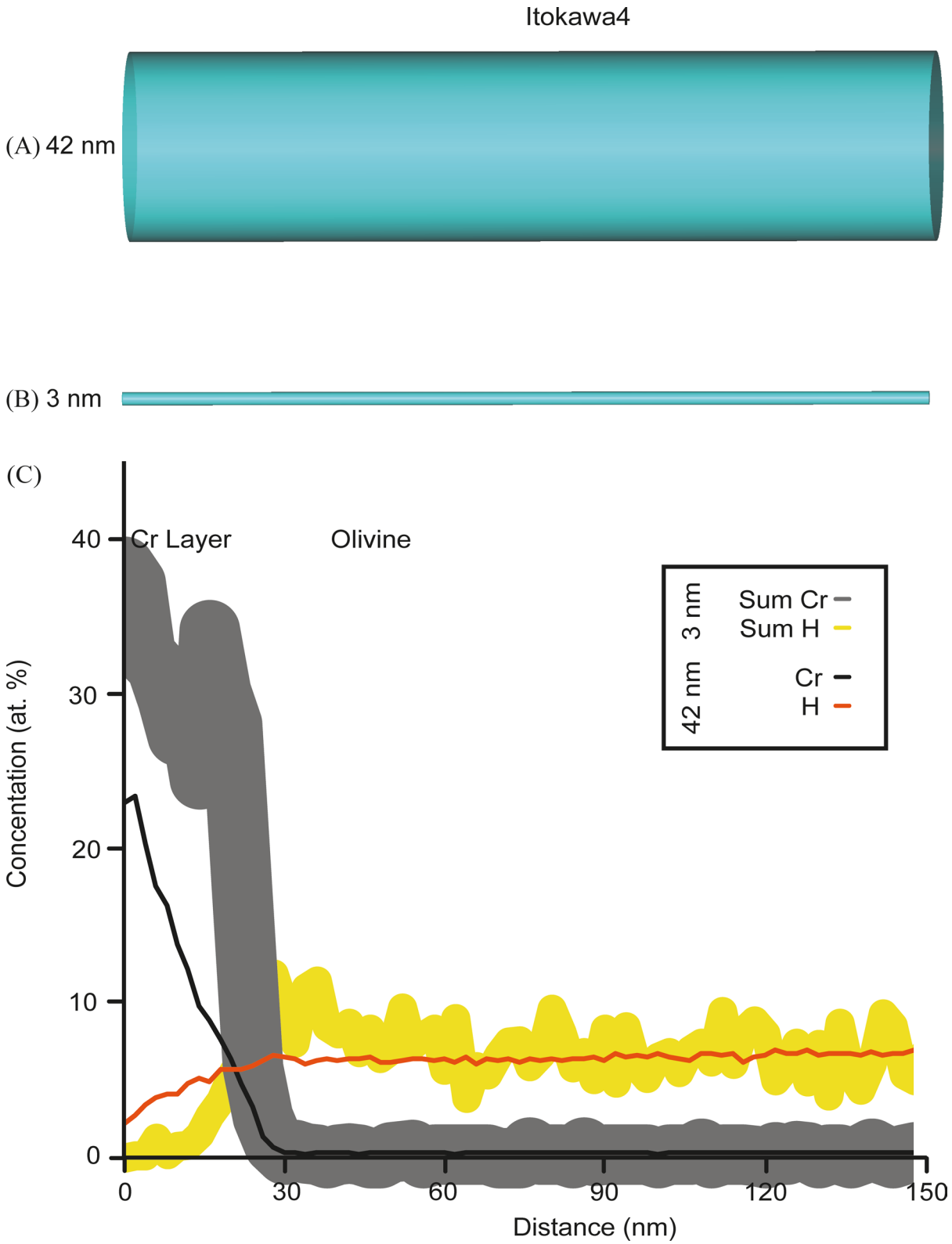

Extended Data Fig. 5 | The effect that changing the diameter of the cylindrical region of interest has on the sputter coated Cr and olivine interface and on counting statistics under the peak. a, The 42 nm cylindrical region of interest used to produce the concentration profiles from the APT dataset Itokawa3 Extended Data Fig. 3J-L. **b**, A 3 nm cylindrical region of interest from the APT dataset Itokawa3. **c**, Corresponding concentration profiles in atomic percent (at. %) for Cr (black line) and H (red line) from the 42 nm region of interest and sum Cr (grey line) and H (yellow line; including molecular ions) concentration profiles from the 3 nm wide cylinder. We note that the Cr-olivine interface is sharper in the 3 nm wide cylinder but it comes at the expense of the counting statistical uncertainty of the measurement. Line widths have been adjusted to represent the 1 sigma uncertainty and depth profiles are absolute abundances not relative concentrations.

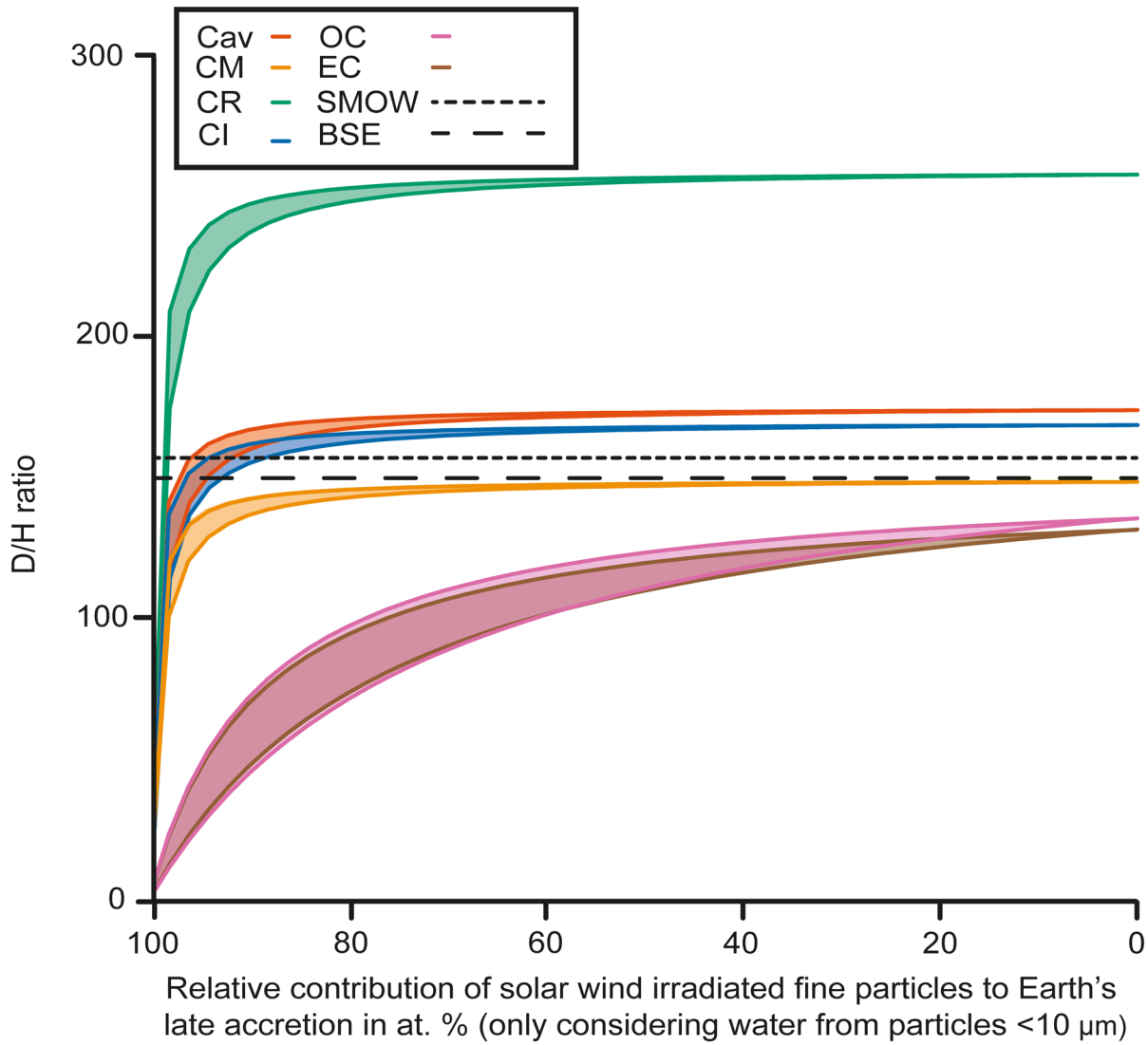

Extended Data Fig. 6 | Diagram of the D/H ratio that results from mixing solar wind irradiated <10 μm fine grained particles and chondritic water reservoirs. The D/H ratio plot is generated by mixing water reservoirs of carbonaceous chondrite (CR[green volume], CI [blue volume], CM [orange volume], Cav [red volume, the average of CR,CI and CMs D/H = 0.000173[1,16]]; water abundance = 2-16 molecular % per atom[9]]), ordinary chondrite (purple volume, OC)19 and enstatite chondrite (brown volume, EC)10 material, and small space weathered particles, where only particles <10 μm that make up ~10 % of present day fine grained extraterrestrial dust are considered (D/H = 0.0000002[24] water abundance = 0.1-1.6 molecular % per atom that can reproduce the SMOW and Bulk Silicate Earth (BSE) D/H ratio[1,17] (horizontal black dashed lines, Supplementary Data 3). The upper and lower bounds of each field represent the upper and lower limits of the water content within the chondrites and solar wind irradiated particles. The relative mass contributions that span BSE and SMOW D/H ratios indicates the range of potential mixtures of theses extraterrestrial water reservoirs that could generate the present-day D/H of Earth's oceans.

Specimen/Data Set	R80_02208	R80_02210	R80_02312	R80_02329	R80_02334	R80_03028	R80_03029	R80_03030
	Itokawa1	Itokawa2	Itokawa4	Itokawa3	PSCO	DSCO1	DSCO2	DSCO3
Instrument Model	**LEAP 4000 XHR**	**LEAP 4000 XHR**	**LEAP 4000 XHR**	**LEAP 4000 XHR**	**LEAP 4000 XHR**	**LEAP 4000 XHR**	**LEAP 4000 XHR**	**LEAP 4000 XHR**
Instrument Settings								
Laser Wavelength (nm)	355	355	355	355	355	355	355	355
Laser Pulse Energy (pJ)	400	300	400	400	400	400	300	300
Pulse Frequency (kHz)	200	125	125	125	200	200	200	200
Evaporation Control	Detection Rate	Detection Rate	Detection Rate	Detection Rate	Detection Rate	Detection Rate	Detection Rate	Detection Rate
Target Detection Rate (ions/pulse)	0.5	0.5	0.5	0.5	0.5	0.5	0.5	0.5
Nominal Flight Path (mm)	382	382	382	382	382	382	382	382
Set Point Temperature (K)	60	60	60	60	60	60	60	60
Sample Temperature (K)	67.9	69.1	69.2	69.2	69.2	69.1	69.1	69.2
Chamber Pressure (Torr)	3.0×10^{-10}	1.6×10^{-10}	1.6×10^{-10}	1.6×10^{-10}	1.7×10^{-10}	4.9×10^{-11}	4.4×10^{-11}	4.2×10^{-11}
Data Summary								
LAS Root Version	18.44.416	18.44.416	15.43.393	18.44.416	15.43.393	18.44.416	18.44.416	18.44.416
CAMECAROOT Version	18.44.416	18.44.416	15.43.393	18.44.416	15.43.393	18.44.416	18.44.416	18.44.416
Analysis Software	IVAS 3.8.2	IVAS 3.8.2	IVAS 3.8.2	IVAS 3.8.2	IVAS 3.8.2	IVAS 3.8.2	IVAS 3.8.2	IVAS 3.8.2
Total Ions:	55918543	51550789	51069268	77491016	60000959	21507053	5000812	21668609
Single	48253959	43737225	44942558	65783571	50483331	18360890	42122192	17966225
Multiple	7248032	7377603	5693858	11062080	9100576	3046130	7654236	3597380
Partial	416552	435961	432852	645365	417052	100033	224384	105004
Reconstructed Ions:								
Ranged	48552545	44014826	39780927	60380691	48116301	18408554	41915694	17609376
Unranged	4320667	4710687	5795260	13059687	8195896	1639735	5019605	2287405
Reconstruction								
Final specimen state	Fractured	Fractured	Fractured	Intact	Fractured	Fractured	Intact	Intact
Pre-/Post-analysis Imaging	FIB-SEM	FIB-SEM	FIB-SEM	FIB-SEM	FIB-SEM	FIB-SEM	FIB-SEM	FIB-SEM
Radius Evolution Model	36.83	12.12	40	38.88	60	57.81	40	50
Field Factor (k)	3.3	3.3	3.3	3.3	3.3	3.3	3.3	3.3
Image Compression Factor	1.65	1.65	1.65	1.65	1.65	1.65	1.65	1.65
Assumed E-Field (V/nm)	21	21	21	30	21	21	21	21

Extended Data Fig. 7 | Operating conditions of the geoscience atom probe (R80). The run number for each sample and sample label are given.

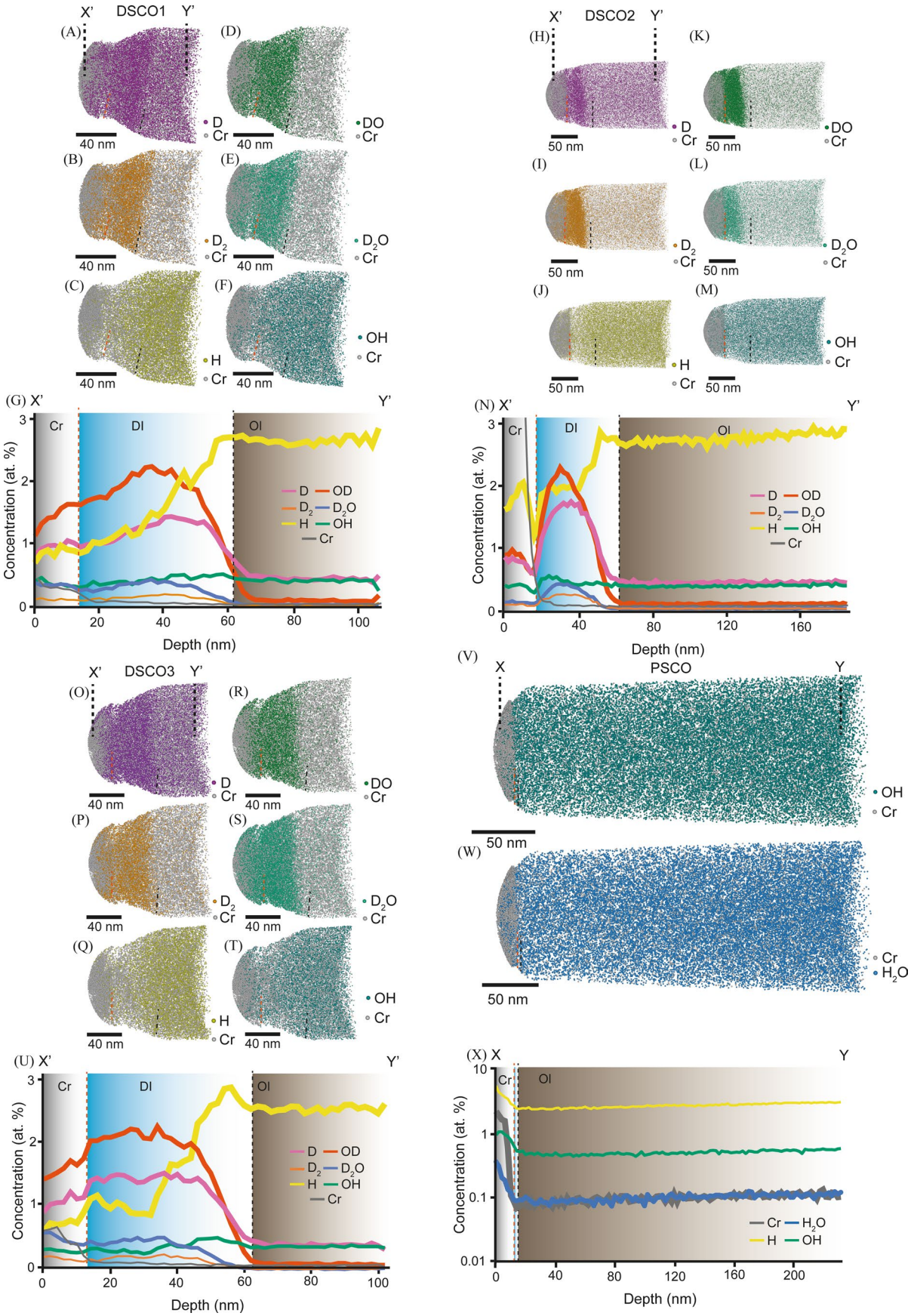

Extended Data Fig. 8 | See next page for caption.

Extended Data Fig. 8 | APT data from DSCO and PSCO standards. DSCO APT data sets (**A**-**U**) initially ran through the Cr protective layer (grey spheres) through DSCO's D-irradiated surface into unweathered olivine. (**A**, **H**, and **O**) APT measurements of the 3D distribution of Cr (grey spheres) and D (purple spheres) ions. (**B**, **I**, and **P**) APT measurements of the 3D distribution of Cr (grey spheres) and D_2 (orange spheres) ions. (**C**, **J**, and **Q**) APT measurements of the 3D distribution of Cr (grey spheres) and H (yellow spheres) ions. (**D**, **K**, and **R**) APT measurements of the 3D distribution of Cr (grey spheres) and DO (green spheres) ions. (**E**, **L**, and **S**) APT measurement of the 3D distribution of Cr (grey spheres) and D_2O (turquoise spheres) ions. (**F**, **M**, and **T**) APT measurements of the 3D distribution of Cr (grey spheres) and OH (teal spheres) ions. (**G**, **N**, and **U**) Concentration of ions in atomic percent (at. %) with depth across the Cr capping layer (Cr, grey shaded region), Deuterium irradiated rim (DI, blue shaded region) and the non-Deuterium irradiated olivine (OI, brown shaded region) revealing the variation in the abundance of Cr (grey line), D (purple line), D_2 (orange line), DO (red line), D_2O (blue line), H (yellow line), and OH (green line) ions. Line widths have been adjusted to represent the 1 sigma uncertainty and depth profiles are absolute abundances not relative concentrations (Supplementary Data 1). The boundary between the Cr and DI layer is marked by a vertical dashed red line and the boundary between the DI and OI layer is marked by a vertical black dashed line. PSCO APT (**V**–**X**) data initially ran through the Cr protective layer (grey spheres) into unweathered olivine. (**V**) APT measurements of the 3D distribution of Cr (grey spheres) and OH (teal spheres) ions. **W**) APT measurements of the 3D distribution of Cr (grey spheres) and H_2O (blue spheres) ions. **X**) Concentration of ions in at. % with depth across the Cr capping layer (Cr, grey shaded region), into the olivine (OI, brown shaded region) revealing the variation in the abundance of Cr (grey line), OH (green line) and H_2O (blue line) ions. Line widths have been adjusted to represent the 1 sigma uncertainty and depth profiles are absolute abundances not relative concentrations (Supplementary Data 1). The boundary between the Cr and OI layer is marked by a vertical dashed red and black line.